

Synchrotron radiation reveals transient weakening during mineral phase transformations

Andrew J. Cross^{1*}, Rellie M. Goddard^{1,2}, Kathryn M. Kumamoto³, David L. Goldsby⁴, Lars N. Hansen⁵, Haiyan Chen⁶, Diede Hein⁵, Christopher A. Thom⁷, M. Adaire Nehring⁵

¹ Department of Geology and Geophysics, Woods Hole Oceanographic Institution; Woods Hole, MA 02532, USA

² Department of Geology, Lakehead University; Thunder Bay, ON, P7B 5E1, Canada

³ Lawrence Livermore National Laboratory; Livermore, CA 94550, USA

⁴ Department of Earth and Environmental Science, University of Pennsylvania; Philadelphia, PA 19104, USA

⁵ Department of Earth and Environmental Sciences, University of Minnesota Twin Cities; Minneapolis, MN 55455, USA

⁶ Mineral Physics Institute, Stony Brook University; Stony Brook, NY 11794, USA

⁷ Rhenium Alloys, Inc.; North Ridgeville, OH 44035, USA

*Corresponding author. Email: across@whoi.edu

1 **Abstract**

2 Phase transformations are widely invoked as a source of rheological weakening during
3 subduction, continental collision, mantle convection, and various other geodynamic phenomena.
4 However, the likelihood and magnitude of such weakening in nature remains undetermined.
5 Here, experiments performed on a synchrotron beamline reveal dramatic weakening across the
6 polymorphic quartz↔coesite phase transition. Under non-hydrostatic conditions, we observe a
7 transient decrease in effective viscosity of up to two orders of magnitude. Such weakening
8 occurs only when the transformation outpaces deformation. We suggest that this behavior is
9 broadly applicable among silicate minerals and examine the likelihood of slab weakening due to
10 the olivine-spinel phase transformation. Our model suggests that cold, wet slabs are most
11 susceptible to transformational weakening, consistent with geophysical observations of slab
12 stagnation beneath the western Pacific.

13

14

15 **Main Text**

16 Rocks and minerals undergo a myriad of solid-state phase transformations during their burial and
17 exhumation through Earth's interior. Notable examples include the transition from quartz to
18 coesite during continental collision, olivine to spinel within the mantle transition zone, and
19 perovskite to post-perovskite near the core-mantle boundary. Such transitions are thought to
20 produce mechanical weakening through various processes. For example, rapid changes in
21 volume (1) and elastic properties (2) can generate internal stresses large enough to induce brittle
22 damage, a potential mechanism for nucleating deep-focus earthquakes (1, 3). Phase
23 transformations can also cause rheological weakening under conditions that preclude brittle
24 failure. Of particular interest are the phenomena of structural superplasticity and transformation

25 plasticity. Structural superplasticity (*i.e.*, grain-size sensitive creep) arises from the formation of
26 fine-grained transformation products that impart long-lived weakening (4, 5). Transformation
27 plasticity on the other hand, though often loosely defined, involves transient weakening during a
28 solid-state phase transformation (6–9), manifested either as a strain rate increase (10) or as a
29 stress drop (11). However, various other characteristics have been attributed to transformation
30 plasticity, including: ‘excess’ plastic deformation produced during a phase transformation, even
31 when the applied stress does not exceed the yield stress (6, 8, 12); anisotropy of the
32 transformation volume change (13); and proportionality between the magnitude of excess
33 straining and the applied stress, volume change, and transformation kinetics (6, 9). Such effects
34 are commonly ascribed to dislocation flux driven by internal stress heterogeneity.

35

36 Transformation plasticity has been invoked across a variety of geodynamic contexts—including
37 mantle convection (14, 15), subduction (16, 17), crustal deformation (9, 18), and mantle plume
38 upwelling (7)—and has even been suggested as perhaps “*the primary deformation mechanism in*
39 *the crust as well as in most of the upper mantle between 400 and 800 km*” (9). Nevertheless,
40 transformation plasticity has proven difficult to examine in the laboratory due to the technical
41 challenges associated with resolving transient effects *in situ*, particularly at elevated temperatures
42 and pressures. As such, most experimental studies to date have focused on phase transformations
43 that occur at ambient pressure (10, 13, 19, 20), often in rock analogs (8, 11, 21).

44

45 To explore the transient rheological effects of phase transformations at more Earth-relevant
46 conditions, deformation-DIA (D-DIA) experiments were performed on a synchrotron beamline
47 to examine the quartz↔coesite (SiO₂) phase transition *in situ*. We chose to study SiO₂ for three
48 primary reasons: first, its abundance in Earth’s crust; second, the relative accessibility of the

49 quartz↔coesite transition; and third, as a model (analog) system for other silicate minerals (e.g.,
50 olivine). Two types of experiment were performed. In hydrostatic (control) runs, SiO₂ samples
51 were pressurized from the quartz to the coesite stability field under isothermal conditions.
52 Confining pressure, differential stress, and mineral phase proportions were monitored
53 continuously using energy dispersive X-ray diffraction (XRD), while axial and volumetric strain
54 were measured via X-ray radiography (see *Materials and Methods* for full details). After the
55 sample had fully transformed to coesite, pressure was lowered to induce the reverse, coesite-to-
56 quartz phase transformation. In non-hydrostatic (test) runs, the same procedure was followed
57 while simultaneously deforming the sample via uniaxial shortening. Non-hydrostatic
58 experiments were performed at various temperatures and deformation rates (Table S1). As a
59 reference standard and stress sensor, each experimental assembly also contained a fine-grained,
60 polycrystalline aggregate of San Carlos olivine (Fo₉₀), which did not undergo a phase
61 transformation over the range of experimental conditions explored here. The experiment
62 procedure is detailed in the *Materials and Methods*.

63

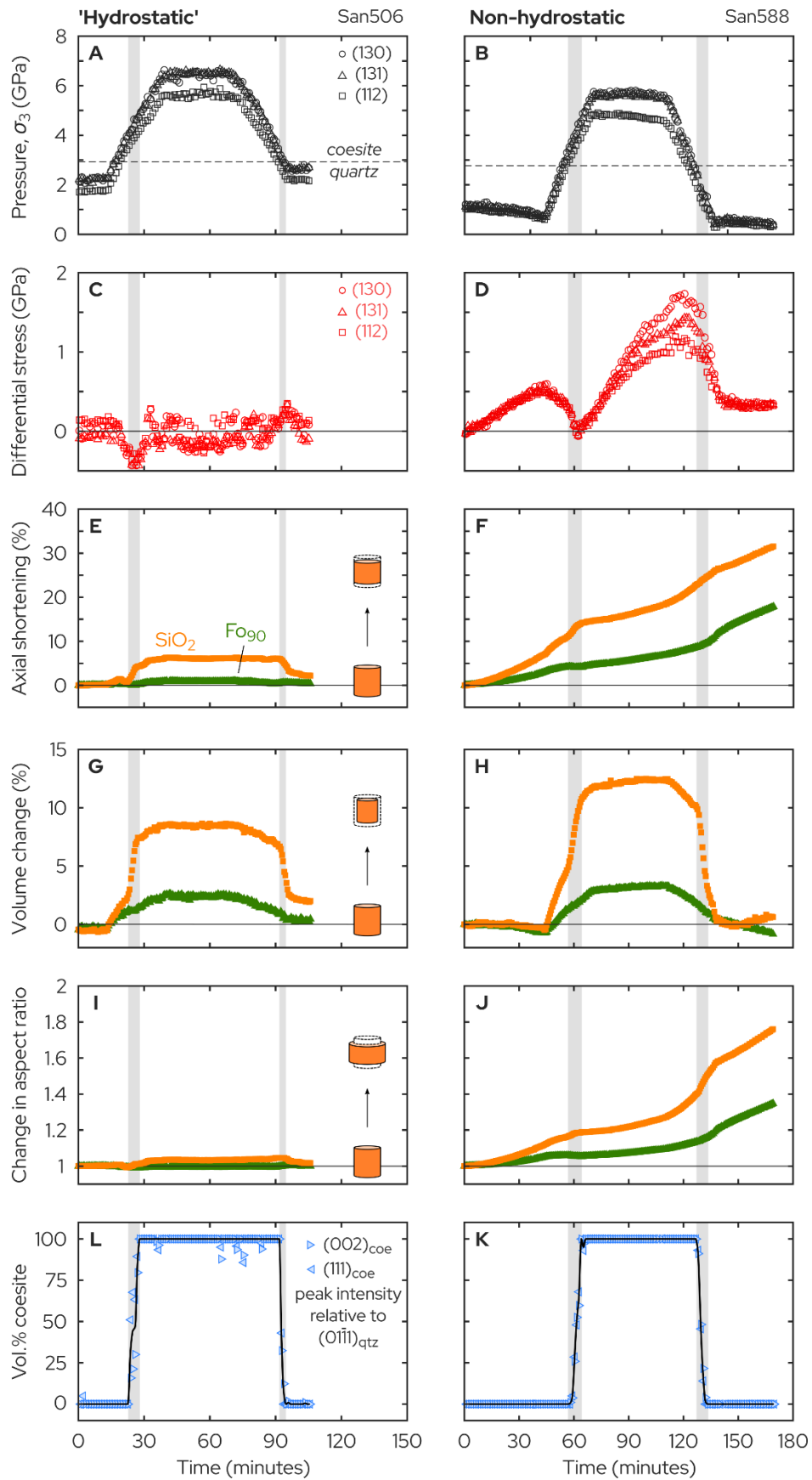
64 **Results**

65 Fig. 1 shows the mechanical evolution of our samples when pressure-cycled across the
66 quartz↔coesite phase transition under hydrostatic versus non-hydrostatic conditions. Under
67 hydrostatic conditions, the Fo₉₀ reference standard undergoes a gradual volume reduction of
68 3.7% during pressurization from the quartz to coesite stability fields (Fig. 1G, green triangles).
69 This volume reduction is almost completely reversed during decompression back to the quartz
70 stability field—a small (<1%) residual volumetric strain can be accounted for entirely by elastic
71 effects, considering the difference between the initial and final confining pressures (Fig. 1A).
72 The Fo₉₀ volume change is isotropic, such that sample shape remains constant throughout the

73 experiment (Fig. 1I). Initially, the SiO₂ sample undergoes a similar gradual volume reduction
74 during pressurization, though larger in magnitude due to the greater compressibility (*i.e.*, smaller
75 bulk modulus) of quartz. However, upon reaching a confining pressure of 3–4 GPa, there is a
76 sharp reduction in volume of ~6% (Fig. 1G, orange squares) coinciding with the emergence of
77 coesite XRD peaks and concomitant loss of quartz XRD peaks (Fig. 1L). During this period,
78 differential stress decreases by 400–500 MPa, placing the sample in deviatoric tension along the
79 vertical axis. Meanwhile, the phase transition introduces a small flattening strain (Fig. 1I) with
80 50% of the SiO₂ volume change accommodated along the vertical axis (greater than the 33%
81 axial strain expected for a perfectly isotropic volume change). Nevertheless, this flattening strain
82 is reversed upon passing back through the coesite-to-quartz phase transition (Fig. 1I), producing
83 no net change in sample shape and only a small residual axial strain (~2%; Fig. 1E) and
84 volumetric strain (~2%; Fig. 1G). We likewise attribute these residual strains to the difference in
85 confining pressure between the start and end of the experiment.

86
87
88
89
90
91
92
93
94
95
96

97 **Fig. 1. Mechanical evolution under hydrostatic versus non-hydrostatic conditions.** (A–B)
98 Confining pressure, σ_3 , (C–D) differential stress, $\sigma_1 - \sigma_3$, (E–F) axial strain, (G–H) volumetric
99 strain, (I–J) sample aspect ratio (diameter divided by height) relative to the initial sample shape,
100 and (L–K) coesite volume proportion as a function of time, calculated from the relative
101 intensities of quartz and coesite diffraction peaks (see *Materials and Methods*). Vertical gray
102 bars represent the time intervals over which both quartz and coesite peaks are present in the XRD
103 spectra. Orange squares and green triangles represent the SiO₂ sample and Fo₉₀ reference
104 standard, respectively, in (E–J).



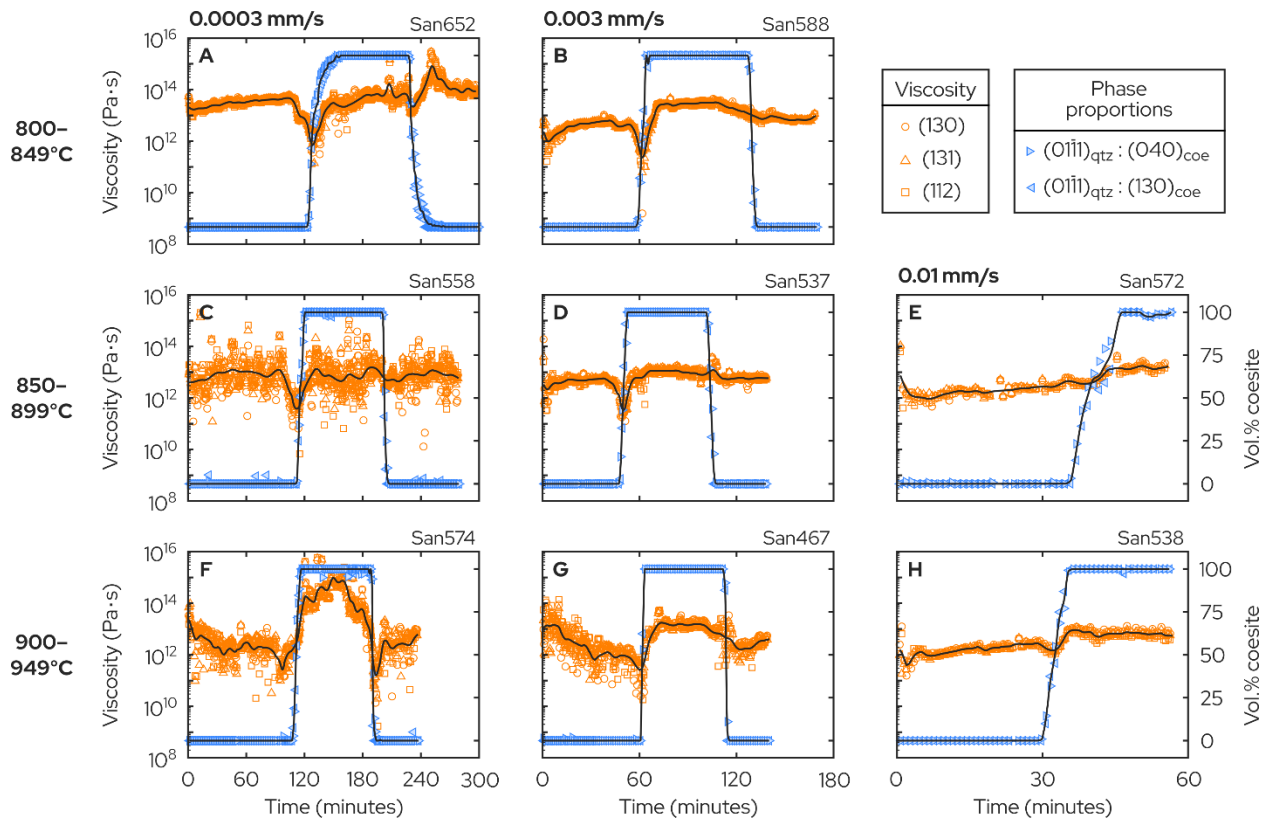
106 Under non-hydrostatic conditions, both the SiO₂ and Fo₉₀ samples undergo continuous isochoric
107 flattening due to the imposed uniaxial shortening (Figs. 1F, 1J). A steady-state strain rate of 4.5
108 $\times 10^{-5} \text{ s}^{-1}$ is reached in the quartz sample after ~4% axial shortening, while differential stress
109 continues to increase into the range of several hundred MPa. After reaching an axial strain of
110 8%, we start increasing confining pressure to induce the quartz-to-coesite phase transition. As
111 before, the phase transition produces a rapid ~6% volume decrease in the SiO₂ sample (Fig. 1H),
112 50% of which is accommodated along the compression axis (Fig. 1F). At the same time, the
113 applied differential stress completely relaxes, placing the sample under a deviatoric tensional
114 stress of 50–60 MPa along the compression axis at the mid-point of the phase transition (Fig.
115 1B). Thereafter, differential stress begins increasing to place the sample back into a compressive
116 stress regime, approaching a steady-state value of 1.0–1.5 GPa in the coesite stability field.

117
118 The most marked differences between the hydrostatic and non-hydrostatic experiments are
119 observed during depressurization and the associated coesite-to-quartz transition. Whereas the
120 SiO₂ sample became unflattened during depressurization in the hydrostatic experiment (Fig. 1E),
121 we observe significant additional flattening during the non-hydrostatic coesite-to-quartz
122 transition (Fig. 1J), despite the sharp increase in sample volume (Fig. 1H). X-ray radiographs
123 reveal that the SiO₂ sample—instead of lengthening, as in the hydrostatic experiment—
124 accommodates the volume increase by expanding perpendicular to the compression axis (*i.e.*,
125 parallel to the minimum principal stress, σ_3 , axis). This observation is common to all of our non-
126 hydrostatic experiments and reflects a “biasing” (anisotropy) of the volume change due to the
127 presence of a differential stress, which, in this case, relaxes gradually by ~1 GPa during the
128 coesite-quartz transition, remaining compressive throughout (Fig. 1D). Interestingly, the Fo₉₀
129 reference standard begins deforming five times faster towards the end of the coesite-quartz

130 transition, before returning to a lower strain rate in the quartz stability field (Fig. 1F). Again, this
131 observation is common among our non-hydrostatic experiments, and is attributed to internal
132 stresses generated by the SiO₂ volume increase within our deformation assembly (in effect, the
133 SiO₂ sample pushing against the Fo₉₀ sample as it expands). Internal stresses may also explain
134 the lack of a dramatic stress drop during the coesite-to-quartz transition, such as that seen during
135 the quartz-to-coesite transition.

136
137 To assess the effect of deformation conditions on the magnitude of transient weakening, we
138 performed non-hydrostatic experiments at nominal temperatures in the range 800–950°C, and
139 differential ram displacement rates corresponding to SiO₂ axial strain rates in the range 10⁻⁷–10⁻⁴
140 s⁻¹ (see *Materials and Methods*). Fig. 2 shows SiO₂ sample viscosity as a function of time,
141 alongside the volume proportion of coesite through time. During the quartz→coesite
142 transformation, we observe marked transient weakening under most conditions, manifested as a
143 short-lived decrease in SiO₂ sample viscosity (*e.g.*, Fig. 2A). These viscosity drops coincide with
144 the point at which there is a roughly 50-50 vol.% mixture of quartz and coesite—in other words,
145 the point at which the phase transformation is proceeding most rapidly. While the magnitude of
146 transient weakening is not clearly temperature-dependent—compare, for example, Figs. 2A, C,
147 and F—we do observe a strong strain-rate dependence. At the lowest deformation rate (0.0003
148 mm/s differential ram syringe pump rate), the SiO₂ sample becomes 1–2 orders of magnitude
149 weaker during the quartz→coesite transition (Figs. 2, left column), whereas scarcely any
150 weakening is detected at the highest deformation rate (0.01 mm/s differential ram syringe pump
151 rate; Figs. 2, right column). The reverse, coesite→quartz transformation, on the other hand,
152 produces no significant or systematic change in viscosity in most experiments. One notable
153 exception is experiment San574, conducted at the highest temperature and lowest strain rate, in

154 which the coesite→quartz transformation produces more than a tenfold reduction in viscosity
 155 (Fig. 2F). In this experiment, the sample went into deviatoric tension during the quartz→coesite
 156 transformation, and back to deviatoric compression during the coesite→quartz transformation—
 157 the observed viscosity drops reflect these changes between positive to negative differential
 158 stresses (*i.e.*, passing through zero differential stress).
 159



160

161 **Fig. 2. Viscosity evolution as a function of temperature (top to bottom) and deformation**
 162 **rate (left to right).** Each experiment was performed under a nominally constant temperature
 163 within the indicated ranges. Viscosity (orange symbols) is calculated from the first time-
 164 derivative of the SiO₂ axial strain (*i.e.*, strain rate) and differential stress from three diffraction
 165 peaks in the Fo₉₀ stress sensor: (130), (131), and (112). As a visual aid, a spline has been fit
 166 through the average of these data (black curve). Also shown (blue symbols) are the volume
 167 proportions of coesite as a function of time, calculated from the relative heights of the (040) and
 168 (130) XRD peaks in coesite and the (01 $\bar{1}$ 1) peak in quartz (see *Materials and Methods*).
 169

169

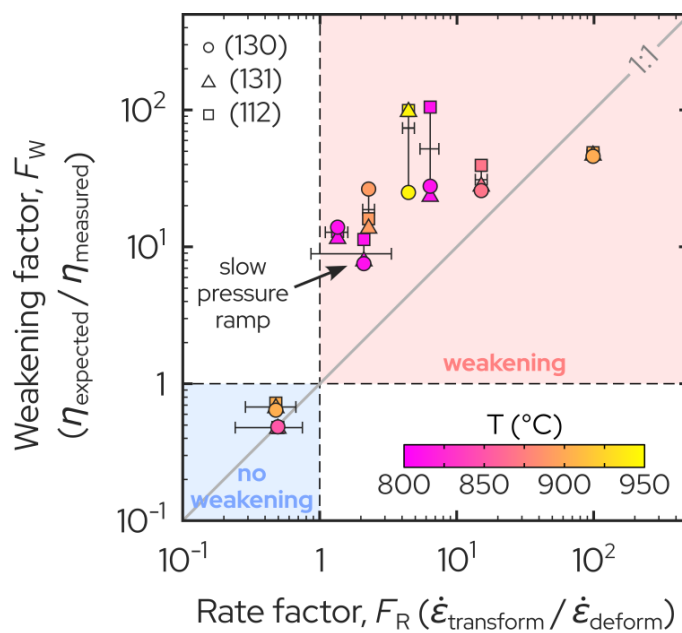
170

171 **Discussion**

172 We propose that transformation-induced weakening in our experiments is primarily governed by
173 a competition between the imposed rate of deformation and the induced rate of phase
174 transformation. Weakening occurs when the phase transformation is rapid relative to the imposed
175 deformation (*i.e.*, at low differential ram rates and strain rates; Figs 2A–F), whereas no
176 weakening occurs when deformation is able to keep pace with the transformation (*i.e.*, at high
177 differential ram rates and strain rates; Figs. 2G–H). Weakening thus arises from an effective
178 (additional) strain rate produced as the sample passes through the phase transition and undergoes
179 a change in volume—an effect predicted by Poirier (9) in a theoretical treatment of
180 transformation plasticity. We illustrate this effect in Fig. 3 by plotting the magnitude of transient
181 weakening, F_W , versus a rate factor, F_R , defined as the ratio between the transformation rate and
182 deformation rate—see the *Supplementary Text* for detailed descriptions. In short, F_W represents
183 the amplitude of the quartz→coesite viscosity drop for each experiment, while F_R is taken as the
184 ratio of the transformation rate (*i.e.*, volumetric strain rate resolved along the compression
185 direction) and deformation rate (*i.e.*, ambient axial strain rate)—see Fig. S6 for a schematic
186 illustration. Both quantities are dimensionless. As expected, weakening occurs only when $F_R > 1$,
187 becoming more pronounced (*i.e.*, increasing F_W) as the transformation increasingly outpaces
188 deformation (*i.e.*, increasing F_R). We note that most experiments fall on a linear trend lying
189 above the 1:1 line between F_W and F_R (Fig. 3). The 1:1 line represents the amount of weakening
190 expected solely from the effective increase in strain rate (due to the volume change)—for
191 instance, if the volume change produces an effective tenfold increase in strain rate along the
192 compression direction, the sample must, by definition, experience a tenfold transient decrease in
193 viscosity. The additional weakening revealed by Fig. 3 arises, at least in part if not entirely, from
194 elastic unloading of the sample as it contracts, causing differential stress to decrease (*e.g.*, Figs.

195 1C–D; (22)) as observed and ascribed to transformation plasticity in experiments on cobalt (11).
196 Other potential sources of weakening are transformational faulting (1), grain size reduction (5),
197 and dislocation nucleation and glide driven by transformation-induced internal stresses (9).
198 Experiments to quantify microstructure evolution across the quartz↔coesite transition are
199 underway and will be presented at a later date. For now, we examine two experimental samples
200 quenched mid-way through the quartz→coesite phase transition: one at ~800°C (San552) and the
201 other at ~900°C (San568), both under non-hydrostatic conditions with 0.003 mm/s differential
202 ram syringe pump rate (Table S1). Backscattered electron images reveal that the samples have
203 undergone 50–90% of the transformation to coesite (Fig. S7). Remnant quartz grains are equant
204 and fine-grained (1–10 μm diameter at 800°C, 10–30 μm diameter at 900°C), whereas coesite
205 forms large needle- (San552; Fig. S7a) or lath-shaped (San568; Fig. S7b) grains, up to 200 μm in
206 length and with aspect ratios frequently >10. Clearly, weakening cannot be explained by grain-
207 size reduction in our experiments. We also do not find any evidence for transformational
208 faulting—only sample San552 contains visible, horizontal cracks, which we attribute to
209 decompression at the end of the experiment. Dislocation analyses are beyond the scope of this
210 study; however, we reiterate that weakening is not strongly temperature-dependent (Figs. 2 and
211 3), which might imply that dislocations play a limited role, given the expected temperature
212 dependence of dislocation recovery (18).

213



214

215 **Fig. 3. Magnitude of transient weakening, F_W , versus the ratio between the rates of**
 216 **transformation and deformation, F_R .** See text for details. Three weakening factors are
 217 calculated for each experiment, one for each F_{090} diffraction peak. Rate factor errors are
 218 calculated assuming conservative uncertainties on the transformation rate, $\Delta\dot{\epsilon}_{\text{transform}}$, and
 219 deformation rate, $\Delta\dot{\epsilon}_{\text{deform}}$ (see *Supplementary Text*). Data points are colored according to
 220 experiment temperature.

221

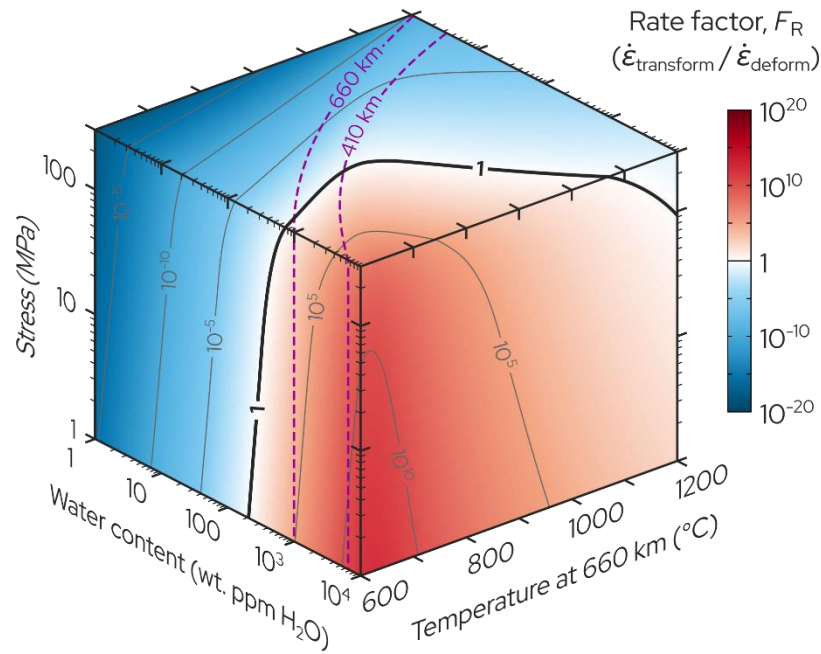
222

223 To assess how our observations scale to longer (geologic) timescales, we performed one
 224 experiment where pressure was ramped an order of magnitude slower than in all other
 225 experiments (San585; Table S1; Fig. S8, middle column). As with all other non-hydrostatic
 226 experiments, the sample experienced a rapid stress drop (Fig. S8E) and transient strain-rate
 227 increase (Fig. S8H) during the quartz→coesite transformation. The only significant difference is
 228 the occurrence of a double viscosity drop (Fig. S8Q) due to the sample passing twice through the
 229 point of zero differential stress: first as the stress state changes from deviatoric compression to
 230 tension near the onset of the transformation, then back to compression upon the completion of
 231 the transformation. Crucially, the magnitude of weakening observed in San585 is entirely
 232 consistent with our other experiments, plotting on the same trend of F_W versus F_R (Fig. 3).

233

234 Having established a scalable rate parameter, F_R , we now seek to interrogate whether phase
235 transformations can produce similar weakening on geologic timescales. As an example, we
236 consider the case of a slab passing through Earth's mantle transition zone, assuming that our
237 findings for SiO_2 are applicable to other mineral systems. Following Hosoya *et al.* (23), we
238 calculate the progression of the olivine-wadsleyite phase transformation for a slab being
239 subducted at a rate of 12 cm/yr, with a thermal gradient of $0.6^\circ\text{C}/\text{km}$, and 5 mm olivine grain
240 size. We vary slab temperature at the 660-km discontinuity between 600°C and 1200°C ,
241 representing the range of cold to hot subduction zones (24), while water content is varied
242 between 1 and 10,000 wt. ppm H_2O to encompass dry to water-saturated conditions (25). The
243 transformation rate, $\dot{\epsilon}_{\text{transform}}$, is taken as one-third of the maximum volumetric strain rate for each
244 set of slab conditions, assuming an isotropic, 10% total volume reduction from olivine to
245 wadsleyite (Fig. S9A). Meanwhile, we calculate slab deformation using rheological flow laws
246 for wet dislocation creep and low-temperature plasticity of olivine (26, 27) for slab stresses up to
247 300 MPa (28–30). The deformation rate, $\dot{\epsilon}_{\text{deform}}$, is taken as the total strain rate at the same depth
248 as $\dot{\epsilon}_{\text{transform}}$ for each set of conditions (Fig. S9B). We neglect the role of intracrystalline
249 (martensitic) nucleation for the olivine-spinel transformation, which is thought to proceed more
250 rapidly than intercrystalline (diffusional) nucleation and growth (30). Thus, our model provides a
251 lower bound on F_R (by underestimating $\dot{\epsilon}_{\text{transform}}$). A detailed description of the model is provided
252 in the *Supplementary Text*.

253



254

255 **Fig. 4. Transformation rate factor, F_R , as a function of water content, temperature, and**
 256 **stress in a subducting slab.** Transient weakening occurs when $F_R > 1$ (white to red shading).
 257 Dashed lines indicate the range of conditions over which the maximum transformation rate (*i.e.*,
 258 the point of maximum weakening) coincides with the mantle transition zone (410–660 km
 259 depth).

260
 261

262 Fig. 4 shows the rate factor, F_R , as a function of water content, temperature, and stress in a
 263 downgoing slab. Due to the highly non-linear nature of both the phase transformation kinetics
 264 and rheological behavior, F_R varies over 30 orders of magnitude, from 10^{-18} to 10^{12} for the range
 265 of conditions explored here. Crucially, we find a large swath of parameter space over which $F_R >$
 266 1—indicating conditions favorable for transient, transformation-induced weakening of the type
 267 seen in our experiments—with more weakening predicted for cold, wet slabs. No weakening is
 268 predicted for slabs in which olivine contains <20 wt. ppm H_2O (<150 wt. ppm H_2O for a slab
 269 stress of 300 MPa). Furthermore, we find that the point of maximum transient weakening (*i.e.*,
 270 the depth at which the phase transformation rate is greatest) coincides with the mantle transition
 271 zone (410–660 km depth) for cold, wet slabs (Fig. 4, dashed lines). These predictions are

272 interesting for two reasons. First, recent water-partitioning experiments have shown that even in
273 wet slabs, olivine will be kinetically dry (containing only ~1 wt. ppm H₂O) when coexisting with
274 hydrous phases (25). Thus, transformational weakening may be triggered by water release upon
275 the thermal breakdown of hydrous phases, with the hydration of olivine enhancing the phase
276 transformation kinetics. Second, seismic tomography studies have revealed that some slabs
277 buckle and stagnate within the mantle transition zone or shallow lower mantle (500–1000 km
278 depth), particularly along the margins of the Pacific plate, where old, cold oceanic lithosphere is
279 subducted (31). Slab stagnation has been ascribed to various phenomena, including heat release
280 during phase transitions (32, 33), mantle viscosity structure (34, 35), trench retreat (36, 37),
281 structural superplasticity (4, 5), and transformation plasticity (15). Our experiments demonstrate
282 that phase transformations can indeed impart a significant, transient decrease in effective
283 viscosity, providing mechanical instability that is consistent with geophysical observations of
284 slab stagnation in cold, wet slabs. Thus, our results highlight the complex coupling between
285 metamorphism and rheological behavior, and provide a quantitative basis for incorporating
286 transformational weakening in future geodynamic simulations.

287 **References and Notes**

- 288 1. H. W. Green II, P. C. Burnley, A new self-organizing mechanism for deep-focus earthquakes. *Nature* **341**, 733–
289 737 (1989).
- 290 2. S. E. Johnson, W. J. Song, A. C. Cook, S. S. Vel, C. C. Gerbi, The quartz $\alpha \leftrightarrow \beta$ phase transition: Does it drive
291 damage and reaction in continental crust? *Earth Planet. Sci. Lett.* **553**, 116622 (2021).
- 292 3. J. Gasc, C. Daigre, A. Moarefvand, D. Deldicque, J. Fauconnier, B. Gardonio, C. Madonna, P. Burnley, A.
293 Schubnel, Deep-focus earthquakes: From high-temperature experiments to cold slabs. *Geology* **50**, 1018–1022
294 (2022).
- 295 4. S. Karato, M. R. Riedel, D. A. Yuen, Rheological structure and deformation of subducted slabs in the mantle
296 transition zone: implications for mantle circulation and deep earthquakes. *Phys. Earth Planet. Inter.* **127**, 83–
297 108 (2001).
- 298 5. A. Mohiuddin, S. Karato, J. Girard, Slab weakening during the olivine to ringwoodite transition in the mantle.
299 *Nat. Geosci.* **13**, 170–174 (2020).
- 300 6. G. W. Greenwood, R. H. Johnson, L. Rotherham, The deformation of metals under small stresses during phase
301 transformations. *Proc. R. Soc. Lond. Ser. Math. Phys. Sci.* **283**, 403–422 (1997).
- 302 7. R. B. Gordon, Observation of crystal plasticity under high pressure with applications to the Earth’s mantle. *J.*
303 *Geophys. Res. 1896-1977* **76**, 1248–1254 (1971).
- 304 8. C. G. Sammis, J. L. Dein, On the possibility of transformational superplasticity in the Earth’s mantle. *J.*
305 *Geophys. Res. 1896-1977* **79**, 2961–2965 (1974).
- 306 9. J. P. Poirier, On transformation plasticity. *J. Geophys. Res. Solid Earth* **87**, 6791–6797 (1982).
- 307 10. A. Sauveur, What is steel? *Min. Metall.* **5**, 465–468 (1924).
- 308 11. M. Zamora, J. P. Poirier, Experiments in anisothermal transformation plasticity: The case of cobalt.
309 Geophysical implications. *Mech. Mater.* **2**, 193–202 (1983).
- 310 12. D. C. Dunand, C. Schuh, D. L. Goldsby, Pressure-Induced Transformation Plasticity of H₂O Ice. *Phys. Rev.*
311 *Lett.* **86**, 668–671 (2001).
- 312 13. A. C. D. Chaklader, Deformation of Quartz Crystals at the Transformation Temperature. *Nature* **197**, 791–792
313 (1963).
- 314 14. D. C. Rubie, A. J. Brearley, Phase Transitions Between β and γ (Mg, Fe)₂SiO₄ in the Earth’s Mantle:
315 Mechanisms and Rheological Implications. *Science* **264**, 1445–1448 (1994).
- 316 15. S. V. Panasyuk, B. H. Hager, A model of transformational superplasticity in the upper mantle. *Geophys. J. Int.*
317 **133**, 741–755 (1998).
- 318 16. L. Ruff, H. Kanamori, Seismic coupling and uncoupling at subduction zones. *Tectonophysics* **99**, 99–117
319 (1983).
- 320 17. W. Mao, S. Zhong, Slab stagnation due to a reduced viscosity layer beneath the mantle transition zone. *Nat.*
321 *Geosci.* **11**, 876–881 (2018).
- 322 18. M. S. Paterson, Creep in transforming polycrystalline materials. *Mech. Mater.* **2**, 103–109 (1983).

- 323 19. R. S. Coe, M. S. Paterson, The α - β Inversion in quartz: A coherent phase transition under nonhydrostatic stress.
324 *J. Geophys. Res. 1896-1977* **74**, 4921–4948 (1969).
- 325 20. P. Gillet, Y. Gérard, C. Willaime, The calcite-aragonite transition: mechanism and microstructures induced by
326 the transformation stresses and strain. *Bull. Minéralogie* **110**, 481–496 (1987).
- 327 21. D. H. Zeuch, S. T. Montgomery, J. D. Keck, Some observations on the effects of shear stress on a polymorphic
328 transformation in perovskite-structured lead-zirconate-titanate ceramic. *J. Geophys. Res. Solid Earth* **98**, 1901–
329 1911 (1993).
- 330 22. Y. Zhou, C. He, J. Song, S. Ma, J. Ma, An experiment study of quartz-coesite transition at differential stress.
331 *Chin. Sci. Bull.* **50**, 446–451 (2005).
- 332 23. T. Hosoya, T. Kubo, E. Ohtani, A. Sano, K. Funakoshi, Water controls the fields of metastable olivine in cold
333 subducting slabs. *Geophys. Res. Lett.* **32** (2005).
- 334 24. S. H. Kirby, S. Stein, E. A. Okal, D. C. Rubie, Metastable mantle phase transformations and deep earthquakes
335 in subducting oceanic lithosphere. *Rev. Geophys.* **34**, 261–306 (1996).
- 336 25. T. Ishii, E. Ohtani, Dry metastable olivine and slab deformation in a wet subducting slab. *Nat. Geosci.* **14**, 526–
337 530 (2021).
- 338 26. G. Hirth, D. Kohlstedt, “Rheology of the Upper Mantle and the Mantle Wedge: A View from the
339 Experimentalists” in *Inside the Subduction Factory* (American Geophysical Union, 2003) *Geophysical*
340 *Monograph Series*, pp. 83–105.
- 341 27. J. M. Warren, L. N. Hansen, Ductile Deformation of the Lithospheric Mantle. *Annu. Rev. Earth Planet. Sci.* **51**,
342 581–609 (2023).
- 343 28. G. F. Davies, Mechanics of subducted lithosphere. *J. Geophys. Res. Solid Earth* **85**, 6304–6318 (1980).
- 344 29. C. R. Bina, Patterns of deep seismicity reflect buoyancy stresses due to phase transitions. *Geophys. Res. Lett.*
345 **24**, 3301–3304 (1997).
- 346 30. A. Mohiuddin, S. Karato, An experimental study of grain-scale microstructure evolution during the olivine–
347 wadsleyite phase transition under nominally “dry” conditions. *Earth Planet. Sci. Lett.* **501**, 128–137 (2018).
- 348 31. Y. Fukao, M. Obayashi, T. Nakakuki, the Deep Slab Project Group, Stagnant Slab: A Review. *Annu. Rev. Earth*
349 *Planet. Sci.* **37**, 19–46 (2009).
- 350 32. U. R. Christensen, D. A. Yuen, Layered convection induced by phase transitions. *J. Geophys. Res. Solid Earth*
351 **90**, 10291–10300 (1985).
- 352 33. P. J. Tackley, D. J. Stevenson, G. A. Glatzmaier, G. Schubert, Effects of an endothermic phase transition at 670
353 km depth in a spherical model of convection in the Earth’s mantle. *Nature* **361**, 699–704 (1993).
- 354 34. M. I. Billen, G. Hirth, Rheologic controls on slab dynamics. *Geochem. Geophys. Geosystems* **8** (2007).
- 355 35. H. Čížková, C. R. Bina, Linked influences on slab stagnation: Interplay between lower mantle viscosity
356 structure, phase transitions, and plate coupling. *Earth Planet. Sci. Lett.* **509**, 88–99 (2019).
- 357 36. U. R. Christensen, The influence of trench migration on slab penetration into the lower mantle. *Earth Planet.*
358 *Sci. Lett.* **140**, 27–39 (1996).
- 359 37. S. Yoshioka, A. Naganoda, Effects of trench migration on fall of stagnant slabs into the lower mantle. *Phys.*
360 *Earth Planet. Inter.* **183**, 321–329 (2010).

- 361 38. W. B. Durham, S. Mei, D. L. Kohlstedt, L. Wang, N. A. Dixon, New measurements of activation volume in
362 olivine under anhydrous conditions. *Phys. Earth Planet. Inter.* **172**, 67–73 (2009).
- 363 39. N. A. Dixon, W. B. Durham, Measurement of Activation Volume for Creep of Dry Olivine at Upper-Mantle
364 Conditions. *J. Geophys. Res. Solid Earth* **123**, 8459–8473 (2018).
- 365 40. Y. Wang, W. B. Durham, I. C. Getting, D. J. Weidner, The deformation-DIA: A new apparatus for high
366 temperature triaxial deformation to pressures up to 15 GPa. *Rev. Sci. Instrum.* **74**, 3002–3011 (2003).
- 367 41. D. J. Weidner, M. T. Vaughan, L. Wang, H. Long, L. Li, N. A. Dixon, W. B. Durham, Precise stress
368 measurements with white synchrotron x rays. *Rev. Sci. Instrum.* **81**, 013903 (2010).
- 369 42. L. N. Hansen, K. M. Kumamoto, C. A. Thom, D. Wallis, W. B. Durham, D. L. Goldsby, T. Breithaupt, C. D.
370 Meyers, D. L. Kohlstedt, Low-Temperature Plasticity in Olivine: Grain Size, Strain Hardening, and the
371 Strength of the Lithosphere. *J. Geophys. Res. Solid Earth* **124**, 5427–5449 (2019).
- 372 43. R. M. Goddard, K. M. Kumamoto, L. N. Hansen, D. Wallis, A. J. Cross, C. A. Thom, Validation of subgrain-
373 size piezometry as a tool for measuring stress in polymineralic rocks. ESS Open Archive [Preprint] (2023).
374 <https://doi.org/10.22541/essoar.169755254.46171679/v1>.
- 375 44. A. K. Singh, C. Balasingh, H. Mao, R. J. Hemley, J. Shu, Analysis of lattice strains measured under
376 nonhydrostatic pressure. *J. Appl. Phys.* **83**, 7567–7575 (1998).
- 377 45. E. H. Abramson, J. M. Brown, L. J. Slutsky, J. Zaug, The elastic constants of San Carlos olivine to 17 GPa. *J.*
378 *Geophys. Res. Solid Earth* **102**, 12253–12263 (1997).
- 379 46. D. G. Isaak, High-temperature elasticity of iron-bearing olivines. *J. Geophys. Res. Solid Earth* **97**, 1871–1885
380 (1992).
- 381 47. Z. Mao, D. Fan, J.-F. Lin, J. Yang, S. N. Tkachev, K. Zhuravlev, V. B. Prakapenka, Elasticity of single-crystal
382 olivine at high pressures and temperatures. *Earth Planet. Sci. Lett.* **426**, 204–215 (2015).
- 383 48. I. Suzuki, Thermal Expansion of Periclase and Olivine, and Their Anharmonic Properties. *J. Phys. Earth* **23**,
384 145–159 (1975).
- 385 49. J. Girard, R. E. Silber, A. Mohiuddin, H. Chen, S. Karato, Development of a Stress Sensor for In-Situ High-
386 Pressure Deformation Experiments Using Radial X-Ray Diffraction. *Minerals* **10**, 166 (2020).
- 387 50. B. Lafuente, R. T. Downs, H. Yang, N. Stone, “The power of databases: The RRUFF project” in *Highlights in*
388 *Mineralogical Crystallography* (2015), pp. 1–29.
- 389 51. P. Raterron, S. Merkel, C. W. Holyoke III, Axial temperature gradient and stress measurements in the
390 deformation-DIA cell using alumina pistons. *Rev. Sci. Instrum.* **84**, 043906 (2013).
- 391 52. T. Nagai, O. Ohtaka, T. Yamanaka, Kinetic studies of the α -quartz-coesite transformation of SiO₂. *Mineral. J.*
392 **19**, 147–154 (1997).
- 393 53. T. Nagai, S. Mori, O. Ohtaka, T. Yamanaka, Nucleation and Growth Kinetics of the α -Quartz-Coesite
394 Transformation Using both Powder and Single Crystal Samples. *Rev. High Press. Sci. Technol.* **7**, 125–127
395 (1998).
- 396 54. H. Morishima, T. Kato, M. Suto, E. Ohtani, S. Urakawa, W. Utsumi, O. Shimomura, T. Kikegawa, The Phase
397 Boundary Between α - and β -Mg₂SiO₄ Determined by in Situ X-ray Observation. *Science* **265**, 1202–1203
398 (1994).

399

400 **Acknowledgments:** The authors thank Leif Togle and Amanda Dillman for providing the quartz
401 and olivine starting materials, respectively. AJC acknowledges salary support from the
402 Investment in Science Program (ISP) and Assistant Scientist Endowment Support (ASES)
403 programs at WHOI. Use of the Advanced Photon Source, Argonne National Laboratory, was
404 supported by the U.S. Department of Energy, Office of Science, Office of Basic Energy
405 Sciences, under Contract No. DE-AC02-06CH11357. Use of the 6BM-B beamline was
406 supported by COMPRES, the Consortium for Materials Properties Research in Earth Sciences,
407 under NSF Cooperative Agreement EAR 16-06856. Portions of this work were performed under
408 the auspices of the U.S. Department of Energy by Lawrence Livermore National Laboratory
409 under Contract DE-AC52-07NA27344. LLNL-JRNL-859365.

410

411 **Funding:**

412 National Science Foundation grant EAR-2023128 (AJC, DLG, LNH)

413 National Science Foundation grant EAR-2003389 (AJC)

414 National Science Foundation grant EAR-1806791 (KMK)

415

416 **Author contributions:**

417 Conceptualization: AJC, DLG

418 Funding Acquisition: AJC, DLG, LNH

419 Investigation: AJC, RMG, KMK, HC, DH, CAT, AN, LNH, DLG,

420 Formal Analysis: AJC, DH

421 Software: KMK, LNH, AJC

422 Writing - Original Draft Preparation: AJC

423 Writing - Review & Editing: AJC, RMG, KMK, DLG, LNH, HC, DH, AN

424

425 **Competing interests:** Authors declare that they have no competing interests.

426

427 **Data and materials availability:** All data and code necessary to understand and assess the
428 conclusions of this manuscript have been uploaded as Supplementary Materials.

429

430 **Supplementary Materials:**

431 Materials and Methods

432 Supplementary Text

433 Figs. S1 to S9

434 Tables S1 to S4

435 Data S1 to S13

1
2
3
4
5
6
7
8
9
10
11
12
13
14
15
16
17
18
19
20
21
22
23
24

Supplementary Materials for

Synchrotron radiation reveals transient weakening during mineral phase transformations

Andrew J. Cross^{1*}, Rellie M. Goddard^{1,2}, Kathryn M. Kumamoto³, David L. Goldsby⁴, Lars N. Hansen⁵, Haiyan Chen⁶, Diede Hein⁵, Christopher A. Thom⁷, M. Adaire Nehring⁵

¹ Department of Geology and Geophysics, Woods Hole Oceanographic Institution; Woods Hole, MA 02532, USA

² Department of Geology, Lakehead University; Thunder Bay, ON P7B 5E1, Canada

³ Lawrence Livermore National Laboratory; Livermore, CA 94550, USA

⁴ Department of Earth and Environmental Science, University of Pennsylvania; Philadelphia, PA 19104, USA

⁵ Department of Earth and Environmental Sciences, University of Minnesota, Twin Cities; Minneapolis, MN 55455, USA

⁶ Mineral Physics Institute, Stony Brook University; Stony Brook, NY 11794, USA

⁷ Rhenium Alloys, Inc.; North Ridgeville, OH 44035, USA

*Corresponding author. Email: across@whoi.edu

25
26
27
28
29
30
31

The PDF file includes:

Materials and Methods

Supplementary Text

Figs. S1 to S9

Tables S1 to S4

32
33
34
35
36

Other Supplementary Materials for this manuscript include the following:

Data S1 to S13

37 **Materials and Methods**

38 Starting Materials

39 Dense polycrystalline aggregates of quartz (SiO_2) were prepared via isostatic hot-pressing of
40 natural quartz sand with 5- μm particle size and >99.5% purity (Min-U-Sil[®] 5, U.S. Silica Corp.).
41 Quartz powders were loaded into a Hot Isostatic Press apparatus at ETH Zurich, and hot-pressed
42 for 36 hours at 1200°C and 200 MPa gas confining pressure. No water was added to the powders
43 prior to hot-pressing. After hot-pressing, samples were cored to 1.10 ± 0.05 mm diameter, and
44 ground to 0.50 ± 0.05 mm height. The mean grain size of the hot-pressed quartz starting material,
45 “LT-QHP”, was 7.0 ± 3.9 μm , determined via electron backscatter diffraction (EBSD) mapping
46 at the Marine Biological Laboratory (Woods Hole, MA). In two early experimental runs
47 (San467, San468), we observed a 4–8% net volume loss within the SiO_2 sample following a two-
48 way traverse of the quartz-coesite phase boundary, which we attribute to pore collapse in the hot-
49 pressed quartz starting material. In all subsequent experiments, we first cold-pressed the sample
50 at room temperature and ~5 GPa confining pressure (to close any pores) before depressurizing to
51 our desired starting pressure of 1–2 GPa. X-ray diffraction (XRD) spectra were collected during
52 some of these cold-presses to verify that the SiO_2 sample remained metastable as quartz.

53

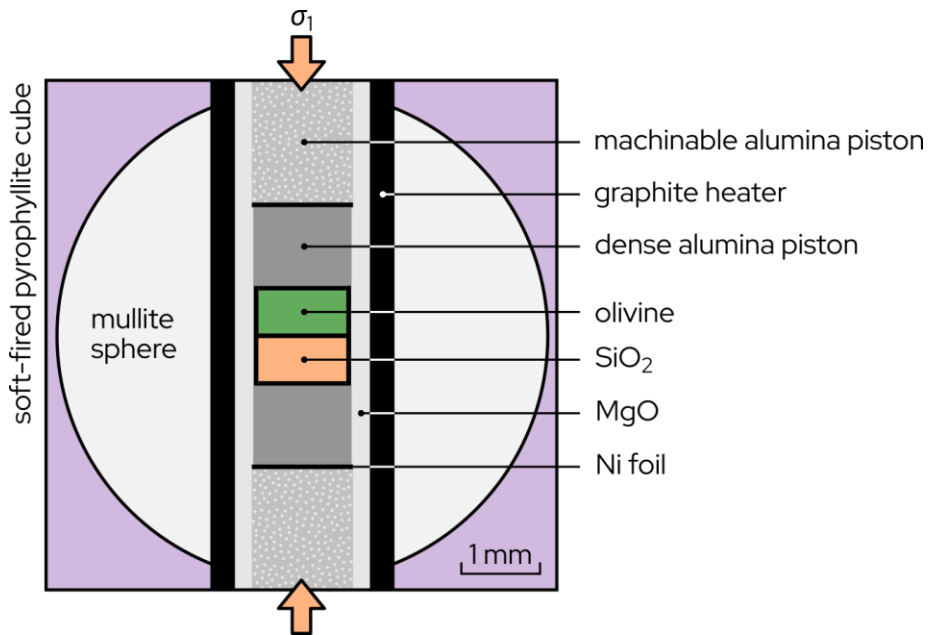
54 Each sample assembly also contained a dense polycrystalline aggregate of hot-pressed San
55 Carlos olivine ($(\text{Mg}_{0.9}\text{Fe}_{0.1})_2\text{SiO}_4$), which was primarily used to calculate stress and pressure *in*
56 *situ* via energy-dispersive XRD (details provided below). However, the olivine aggregate also
57 served as a control sample since it does not undergo any phase transformations over the range of
58 experimental conditions explored here. San Carlos powders with particle size <10 μm containing
59 ~1% orthopyroxene were dried at 1000°C for 12 hours in a gas-mixing furnace with oxygen
60 fugacity set to $\sim 10^{-7}$ Pa. Next, the powders were cold-pressed into a Ni capsule, loaded into a
61 Paterson gas-medium apparatus, and vacuum hot-pressed for 1 hour at 1200–1250°C and 300
62 MPa confining pressure with a vacuum pressure of 10–27 Pa on the interior of the capsule. After
63 hot-pressing, samples were cored and ground to 1.10 ± 0.05 mm diameter and 0.50 ± 0.05 mm
64 height, respectively. Olivine samples were extracted from three such hot-presses: PI-2056, PI-
65 2094 and PT-1616. We note that the powder used for hot-press PI-2094 had a light-gray
66 discoloration, presumably arising from Fe contamination during ball-milling. However, Fe
67 contamination should not affect the elastic properties of olivine. Portions of each hot-press were
68 polished using diamond lapping film down to a grit size of 0.5 μm and finished with a vibratory
69 colloidal silica polish. Polished samples were coated with 5 nm carbon and examined via EBSD
70 at the University of Minnesota on a JEOL JSM 6500F field emission gun scanning electron
71 microscope (FEG-SEM) operating in high-vacuum mode at an accelerating voltage of 20 kV.
72 EBSD maps were collected at step-sizes of 0.5 μm (PI-2056) or 0.1 μm (PI-2094, PT-1616).
73 These maps revealed mean grain sizes (calculated as area-equivalent diameters) of 6.6 ± 3.7 μm ,
74 3.3 ± 1.0 μm and 2.2 ± 1.9 μm for PI-2056, PI-2094 and PT-1616, respectively.

75

76 Sample Assembly

77 All experimental assemblies contained one quartz sample and one olivine sample stacked in
78 series (*i.e.*, on top of one another; Fig. S1). Dense alumina and machinable alumina pistons were
79 placed above and below the stacked samples, with thin Ni disks separating each component for
80 the purpose of tracking axial strain (*i.e.*, sample height) via X-ray radiography. To monitor
81 sample diameter and thereby calculate volumetric strain, the stacked samples were also wrapped
82 in Ni foil. The Ni foil and disks also served to fix oxygen fugacity near the Ni/NiO buffer. The
83 stacked samples and pistons were inserted into a cylindrical MgO sleeve, which itself was
84 contained within a cylindrical graphite resistance heater (“furnace”), a mullite sphere, and a soft-
85 fired pyrophyllite cube with edges 6.1–6.35 mm in length (Fig. S1). The mullite sphere and
86 pyrophyllite cube served as pressure media and provided a dry environment for the samples (38),
87 which were not sealed. After assembly, the components were cemented in place with ZrO₂ paste
88 and dried overnight at 100°C. The assembly did not contain a thermocouple to avoid introducing
89 a source of mechanical instability at high pressure. Instead, temperature was determined using
90 either 1) a calibrated relationship between temperature and furnace power, or 2) the flow strength
91 of olivine and/or the kinetics of the quartz→coesite phase transformation. These methods
92 provide minimal loss of accuracy given the inherently large thermal gradients within the small
93 sample assembly (39). Details on the temperature calibration are provided below.

94



95

96 **Fig. S1. Schematic diagram of the D-DIA cell assembly.** Polycrystalline aggregates of olivine
97 and SiO₂ are stacked in series along the maximum principal stress (σ_1) direction.

98

99

100 Apparatus Details

101 Experiments were performed in a Deformation-DIA (D-DIA) apparatus (40) located on beamline
102 sector 6-BM-B of the Advanced Photon Source synchrotron (Argonne National Laboratory,
103 Chicago, IL). The D-DIA apparatus consists of three orthogonal pairs of anvils sandwiched
104 between an upper and lower guide block, with each anvil in contact with one face of the sample
105 assembly cube. Confining pressure is generated by advancing the main hydraulic ram, which
106 changes the separation distance between the upper and lower guide blocks, advancing the six
107 anvils equally. Meanwhile, deviatoric stress conditions can be imposed by independently moving
108 the vertical pair of anvils, termed “differential rams”. Differential ram motion is controlled by
109 advancing (or retracting) a pair of hydraulic syringe pumps at a specified rate. Constant syringe
110 pump motion does not perfectly translate into constant strain-rate conditions due to
111 compressibility of the hydraulic fluid. Rather, strain rate evolves to steady-state over a period of
112 a few percent strain following each change in experiment conditions (for example, at the start of
113 each experiment, or following a phase transformation). Experiment conditions are summarized in
114 Table S1.

115 In Situ Stress, Strain, and Phase Proportion Measurements

117 Throughout each experiment, synchrotron X-ray radiation was used to calculate stress and
118 quartz-coesite volume proportions via energy-dispersive XRD, and axial and volumetric strain
119 via X-ray radiography. The detector geometry and procedures for calculating stress and strain
120 have been described in detail elsewhere (39, 41–43). In short, XRD data were obtained by
121 directing a $100 \times 100 \mu\text{m}$ white X-ray beam through a gap between the upstream horizontal
122 anvils, into the sample assembly. Diffraction spectra were collected at a downstream array of 10
123 solid-state detectors arranged at fixed azimuths of $\Psi = 0\text{--}270^\circ$ with respect to the horizontal
124 incident beam—see Figure 3 in (39). The detectors, along with a set of conical slits, were
125 positioned such that the X-ray beam was collimated to a Bragg angle of $2\theta \approx 6.5^\circ$. The precise
126 Bragg angle was calibrated approximately once every three experiments (*i.e.*, once per day)
127 using a powdered alumina standard. Each XRD energy peak corresponds to a (*hkl*) plane for
128 which the lattice spacing, d_{HKL} , is obtained using Bragg’s law. Changes in *d*-spacing under load
129 (*i.e.*, lattice strain) provide quantitative constraints on the stress state of a sample via its elastic
130 properties. During uniaxial shortening in the D-DIA, for instance, lattice strain should be greatest
131 in the (horizontal) plane normal to the shortening axis, and smallest in any (vertical) plane
132 containing the shortening axis. Thus, differential stress is given by the difference in d_{HKL} at $\Psi =$
133 0° and $\Psi = 90^\circ$ via the Singh *et al.* (44) formulation of Hooke’s law, which assumes an isostress
134 condition. In this study, differential stress was calculated separately for the (130), (131), and
135 (112) planes in olivine, using the elastic constants for olivine from Abramson *et al.* (45), along
136 with their pressure derivatives (45) and temperature derivatives (46). Meanwhile, mean stress
137 was calculated using a third-order Birch-Murnaghan equation of state for olivine, with values of
138 129.4 GPa and 4.29 for the olivine bulk modulus and its pressure derivative, respectively (45),

139 -0.02 GPa/K for the olivine bulk modulus temperature derivative (47), and the thermal
 140 expansivity of olivine from Suzuki (48). Note that in this study we draw a distinction between
 141 confining pressure, $P = \sigma_3$, and mean stress, $\sigma_m = (\sigma_1 + 2\sigma_3)/3$, wherein we assume that $\sigma_2 = \sigma_3$,
 142 given the axisymmetric deformation geometry. Differential stress is given as $\sigma_d = \sigma_1 - \sigma_3$, for
 143 which positive values indicate deviatoric compression, and negative values indicate deviatoric
 144 tension, assuming that σ_1 (σ_3) is given by the lattice strain along the vertical (horizontal) axis in
 145 the deformation apparatus, parallel (perpendicular) to the uniaxial shortening axis.

146
 147 Diffraction patterns were collected with dwell times of 5–30 seconds, alternating between the
 148 olivine and SiO₂ samples. We calculated stresses and pressures only for olivine, assuming the
 149 stress states in the stacked olivine and SiO₂ samples to be the same—previous workers have
 150 shown this to be a reasonable assumption within experimental uncertainty (42, 43, 49). Due to
 151 the plastic anisotropy of olivine, there is some variation in stress measured using the different
 152 lattice planes. The average range in stress varies from 60–210 MPa for our experiments, with the
 153 (130) peak consistently giving the largest stresses. Previous studies have suggested that the (130)
 154 peak provides the most accurate measure of the bulk stress for olivine aggregates in compression
 155 (43, 49). SiO₂ diffraction patterns were meanwhile used to monitor the quartz↔coesite phase
 156 transformation and estimate the relative volume proportions of those two phases. Volume
 157 proportions were calculated using the relative intensities (heights) of peaks belonging to quartz
 158 and coesite. Since many of the diffraction peaks in quartz and coesite are weak and overlapping,
 159 we limited our analysis to the (01 $\bar{1}$ 1) peak in quartz, and the (002) and (111) peaks in coesite
 160 (Fig. S2). Peaks were tracked in each of the 10 detectors separately, following the subtraction of
 161 any background (long wavelength) intensity variation. To account for detector-to-detector
 162 variations in signal intensity, each spectrum was also normalized to the range 0–1. Phase volume
 163 proportions were calculated for each combination of quartz and coesite peaks as follows:

$$X_C \equiv 1 - X_Q = \frac{I_{Chkl}}{(I_{Chkl} + I_{Qhkl})}$$

(Eqn. S1)

164
 165
 166
 167
 168 where X_C and X_Q are the volume fractions of coesite and quartz, respectively, and I is the mean
 169 normalized intensity of a particular (hkl) peak across all 10 detectors, divided by the maximum
 170 expected intensity of that (hkl) peak from X-ray powder diffraction (Fig. S2). The subscripts “C”
 171 and “Q” denote coesite and quartz, respectively. In practice, the minimum detectable amount of
 172 either phase is $\sim 0.75\%$. Furthermore, in all experiments the two combinations of peaks—(01 $\bar{1}$ 1)
 173 versus (002), and (01 $\bar{1}$ 1) versus (111)—give estimates within 10% of one another at the 2-
 174 sigma level. These sensitivities could be improved by collecting diffraction patterns over longer
 175 dwell times; however, we favored short dwell times to provide better temporal resolution during
 176 the phase transformations. We should also note that the XRD patterns represent only a 100×100
 177 $\times 1000$ μm volume within the center of our samples, corresponding to $\sim 2.5\%$ of the total sample

178 volume. As such, the measured phase proportions may not be fully representative of the entire
179 sample volume, particularly if the phase transformation is heterogeneous (*e.g.*, due to the
180 heterogeneity of nucleation sites, or thermal gradients within the sample). Indeed, sample
181 volume typically evolves over a longer transient period than the XRD patterns alone would
182 indicate.

183

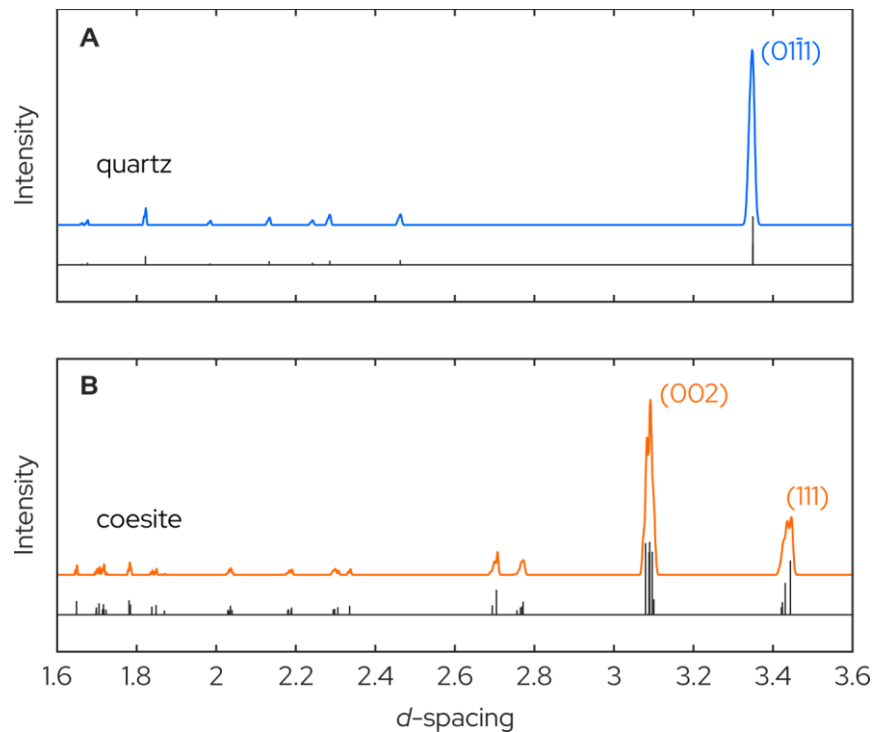
184 Finally, axial and volumetric strain were calculated via digital image cross-correlation of X-ray
185 radiographs collected at 5–30 second intervals throughout each experiment. Interpolation of the
186 X-ray intensity data enabled sub-pixel resolution when tracking the movement of the Ni foils,
187 yielding axial strain resolution down to 10^{-5} and volumetric strain resolution down to 10^{-4} .

188 Volumetric strains were calculated from the two-dimensional X-ray radiographs assuming a
189 cylindrical sample shape, and rotational symmetry of the sample around the compression axis.

190 We estimate that volume strain measurements are accurate within 0–5%, dictated mostly by
191 deviations of the sample from a perfectly cylindrical shape. Axial and volumetric strains are
192 mostly presented here as engineering strains; however, we calculate strain rate and viscosity
193 using true (logarithmic) strains. Shortening strains are reported as positive, while extensional
194 strains are reported as negative.

195

196



197

198

199 **Fig. S2. Calculated X-ray powder diffraction spectra for (A) quartz and (B) coesite.**

200 Expected peak positions shown in black. Data from the RRUFF database (ID R100134 and
201 R070565 for quartz and coesite, respectively) (50).

202 Direct Temperature Calibration

203 The sample assembly used in this study is thermocouple-free for two reasons. First, the presence
204 of a thermocouple introduces mechanical instability, particularly during deformation
205 experiments, due to the large size of the thermocouple relative to the sample assembly. Second,
206 the alumina thermocouple sheath and thermocouple wires act as heat sinks, introducing an
207 additional thermal gradient within the sample assembly—thermal gradients within the small D-
208 DIA assembly volume can exceed 150 K/mm at 1400°C in the presence of a thermocouple (51).
209 Instead, we control temperature using a calibration based on the amount of electrical power
210 supplied to the graphite furnace. It has been argued that this approach is at least as accurate as
211 using a thermocouple (39), provided that the graphite furnace dimensions and material properties
212 are consistent from assembly to assembly.

213
214 The graphite resistance furnaces used in this study were machined at either the University of
215 Oxford, UK (experiments San467–San574) or the University of Minnesota Twin Cities, USA
216 (experiments San585–San652). We hereafter refer to these as “Oxford” and “UMN” furnaces. To
217 determine the power-temperature relationship of our furnaces, we performed a calibration run
218 (San658) using a UMN furnace. Temperature was measured at the center of the sample assembly
219 using a thermocouple (Fig. S3A–B), and monitored as a function of 1) furnace power and 2) the
220 amount of hydraulic load acting on the main ram over a range of 10–50 tons (for context, the
221 experiments described in this paper were conducted at 10–40 tons).

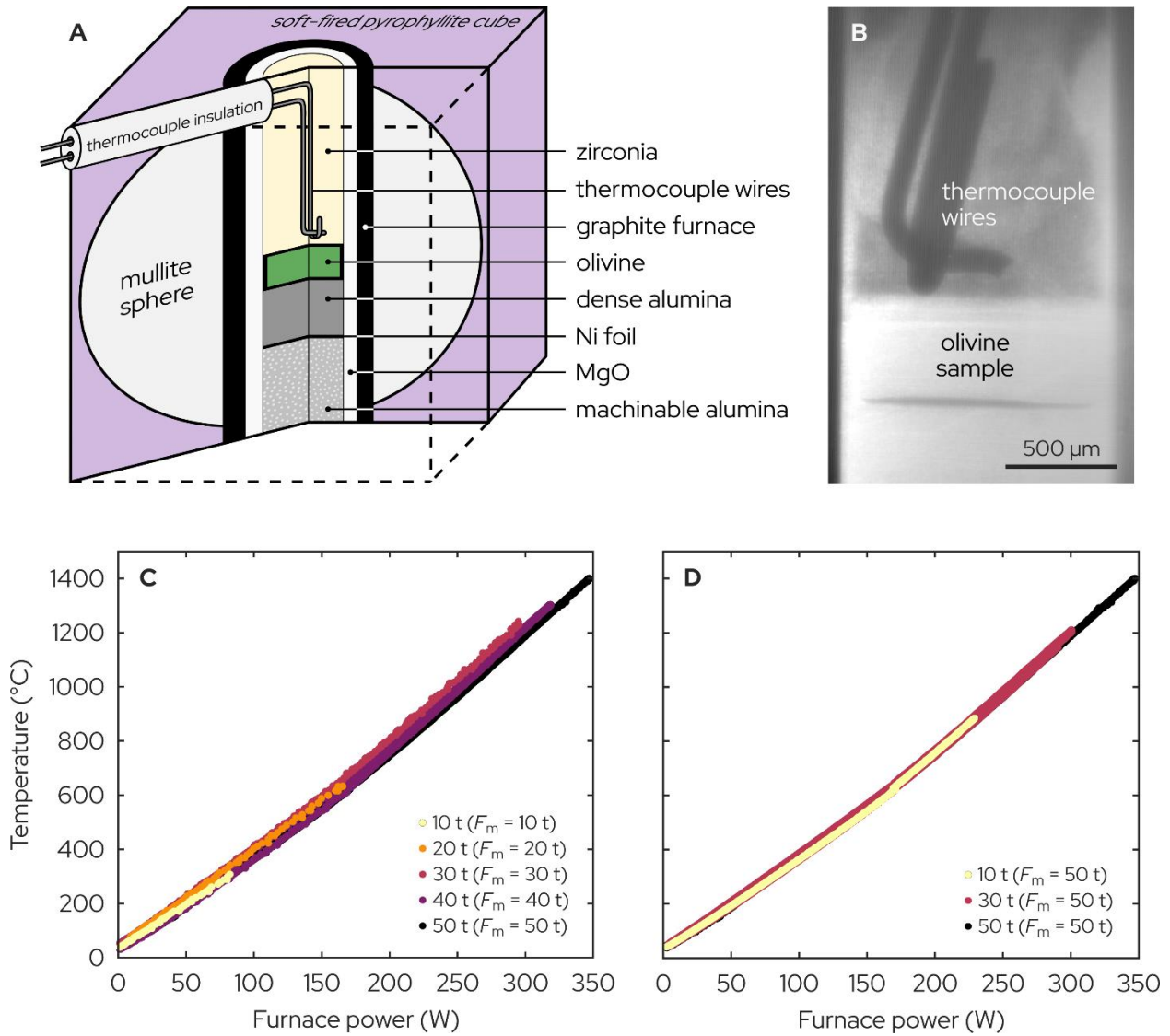
222
223 We find a modest effect of load on the temperature-power relationship. Between 10 and 30 tons,
224 the graphite furnace becomes more efficient with increasing load—in other words, the furnace
225 power required to reach a given temperature decreases—whereas from 30 to 50 tons, the graphite
226 furnace becomes less efficient with increasing load (Fig. S3C). Interestingly, there is also an
227 apparent memory effect, such that furnace efficiency does not evolve with subsequent decreases
228 in load below the maximum attained load, F_m (Fig. S3D). We therefore define a calibration
229 containing two independent variables: furnace power, P (in watts), and the maximum previous
230 load experienced by the sample assembly, F_m (in tons):

$$231$$
$$232 \quad T_{\text{cal}} = B_1 F_m^3 + B_2 P F_m^2 + B_3 P^2 F_m + B_4 P^3 + B_5 F_m^2 + B_6 P F_m + B_7 P^2 + B_8 F_m + B_9 P + B_{10}$$
$$233$$

234 **(Eqn. S2)**

235
236 where $B_1 = 4.44 \times 10^{-3}$, $B_2 = -1.20 \times 10^{-4}$, $B_3 = -3.56 \times 10^{-6}$, $B_4 = -3.37 \times 10^{-6}$, $B_5 = -0.453$,
237 $B_6 = 4.10 \times 10^{-3}$, $B_7 = 4.46 \times 10^{-3}$, $B_8 = 13.6$, $B_9 = 2.96$, and $B_{10} = -61.9$. This fit produces
238 residuals of $\pm 20^\circ\text{C}$ at the 2-sigma level, compared to residuals of $\pm 30^\circ\text{C}$ when the load effect is
239 ignored. Conveniently, with the exception of San467 and San468, all other experiments began
240 with a ~ 5 GPa (40 ton) *in situ* cold press (as described above), such that the maximum load was

241 set at the beginning of each experiment. Furnace efficiency (and, thus, temperature) should have
 242 therefore been constant throughout each experiment, regardless of the imposed changes in load.
 243
 244



245
 246
 247 **Fig. S3. UMN furnace calibration.** (A) Cell assembly for the furnace calibration. (B) X-ray
 248 radiograph showing the position of the thermocouple near the cell center. (C–D) Temperature
 249 versus furnace power. Colors correspond to the main ram load at which each set of
 250 measurements was made. During increments of increasing load, the power-temperature
 251 relationship changes (C); however, when load is subsequently decreased, the power-temperature
 252 relationship no longer evolves (D) and is set according to the maximum load previously
 253 experienced by the sample assembly, F_m .
 254

255 Indirect Temperature Calibration—Quartz↔Coesite Transformation Kinetics

256 Despite being machined to the same nominal dimensions, the UMN and Oxford furnaces do not
257 appear to follow the same power-temperature relationship. First, experiments performed with
258 Oxford furnaces at 167 W furnace power—San537, San538, San558—are weaker than
259 experiments performed with UMN furnaces at 209 W furnace power and comparable strain
260 rates—San585, San588, San652 (Fig. 2). Second, the quartz↔coesite transformation is
261 significantly quicker in the experiments with Oxford furnaces compared to the experiments with
262 UMN furnaces. We therefore infer that experiments San537, San538, and San558 (Oxford
263 furnaces), were actually hotter than experiments San585, San588, and San652 (UMN furnaces),
264 despite the latter operating at greater furnace power.

265
266 In the absence of a suitable power-temperature calibration, we require other means for estimating
267 temperature in experiments containing Oxford furnaces. We tackle this using two independent
268 analyses: the steady-state flow strength of olivine, and the kinetics of the quartz-to-coesite phase
269 transformation.

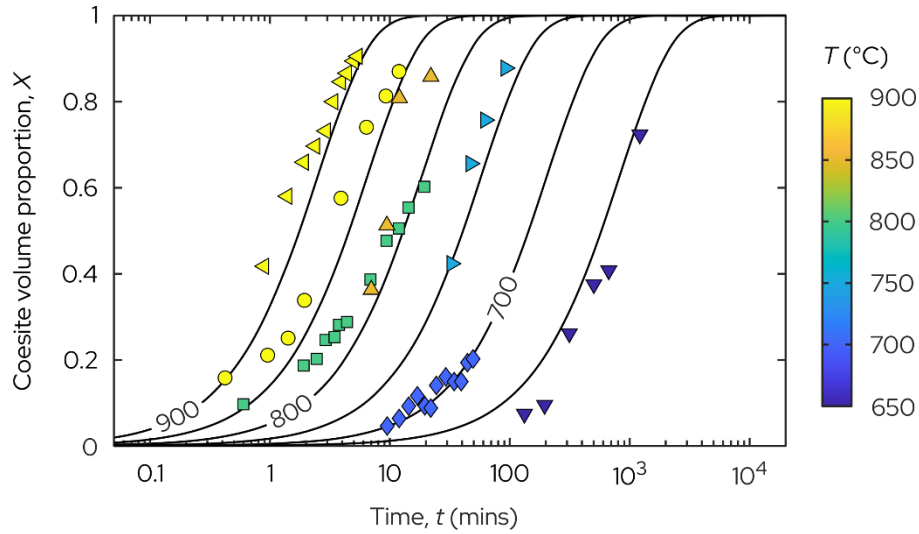
270
271 The quartz→coesite transformation kinetics have already been determined at experimental
272 conditions very similar to ours by Nagai *et al.* (52, 53). First, we refit their data to the Avrami
273 equation (Fig. S4):

274
275
$$X = 1 - \exp(-kt^m) \quad \text{(Eqn. S3)}$$

276
277
$$k = k_0 \exp(-Q/RT) \quad \text{(Eqn. S4)}$$

278
279 where X is the fraction of transformed material, t is time, m is the dimensionless Avrami
280 exponent, and k is a rate parameter expressed as a function of a pre-exponential constant, k_0 , the
281 activation enthalpy of the transformation, Q , the gas constant, R , and absolute temperature, T .
282 This formulation does not account for pressure (or, rather, overpressure). We infer that pressure
283 effects are minimal since the Nagai *et al.* (52, 53) experiments were performed at confining
284 pressures of either 4 or 6 GPa—that is, with either ~1 or ~3 GPa of overstepping—yet conform
285 reasonably well to a single Avrami fit (Fig. S4).

286



287
288

289 **Fig. S4. Quartz→coesite transformation kinetics.** Data are from Nagai *et al.* (1997, 1998),
290 colored according to temperature, and refit using [Eqns. S3–S4](#) with $n = 1$.

291
292

293 As in Nagai *et al.* (52, 53), we fix the Avrami exponent at $n = 1$, which yields values of $\log_{10}(k_0)$
294 $= 16.38 (\pm 1.40) \text{ s}^{-1}$, and $Q = 209 (\pm 12) \text{ kJ mol}^{-1}$, where the uncertainties are given as two
295 standard deviations. Next, we fit our quartz→coesite phase proportion data to the Avrami
296 equation (Eqn. S3) to obtain the rate parameter, k , for each experiment, while again fixing $n = 1$.
297 A “kinetics temperature”, T_{kin} , is then obtained for each experiment via Eqn. S4, using the values
298 of k_0 and Q derived from the Nagai *et al.* (52, 53) data. To estimate the uncertainty on each
299 kinetics temperature, we perform a Monte Carlo analysis where we generate 10^6 random values
300 of the parameters $\log_{10}(k)$, $\log_{10}(k_0)$, and Q , each following a Gaussian distribution of width
301 dictated by the 2-sigma uncertainty for each parameter. These randomly generated values are
302 then used to calculate a range of T_{kin} for each experiment. At the 2-sigma level, these
303 temperatures consistently vary within an uncertainty range of $\pm 50\text{--}60^\circ\text{C}$. The rate parameters,
304 kinetics temperatures, and temperature uncertainties are summarized in Table S2.

305

306 Encouragingly, we note that the UMN-furnace experiments (San585, San588, San652) yield
307 kinetics temperatures (784°C , 805°C , 836°C , respectively) that are remarkably close to the
308 temperature estimated from the UMN power-temperature calibration, $810 \pm 20^\circ\text{C}$, with a mean
309 offset of only -2°C . Moreover, the Oxford-furnace experiments described above (San537,
310 San538, San558) yield kinetics temperatures that are indeed higher (870°C , 841°C , 828°C ,
311 respectively), despite the lower furnace power in those experiments, as inferred above.

312
313
314

315 Indirect Temperature Calibration—Olivine Flow Strength

316 For comparison against the kinetics temperatures described above, we also calculate “flow law
317 temperatures”, T_{flow} , using olivine flow laws of the following general form:

318

$$\dot{\epsilon}_i = A_i \sigma^{n_i} d^{-m_i} \exp\left(-\frac{E_i + PV_i}{RT}\right) \quad (\text{Eqn. S5})$$

320

321 where $\dot{\epsilon}$ is the steady-state strain rate, A is a pre-exponential constant, σ is differential stress, n is
322 the stress exponent, d is grain size, m is the grain-size exponent, E is activation energy, P is
323 confining pressure, V is activation volume, R is the gas constant, T is absolute temperature, and
324 the subscript “i” indicates parameters determined for the i th deformation mechanism. Here, we
325 assume that the total creep rate of our olivine sample is given as:

326

$$\dot{\epsilon} = \dot{\epsilon}_{\text{dis}} + \dot{\epsilon}_{\text{GBS}} + \dot{\epsilon}_{\text{dif}} \quad (\text{Eqn. S6})$$

328

329 where the subscripts “dis”, “GBS”, and “dif” represent dislocation creep, dislocation-
330 accommodated grain boundary sliding (disGBS), and diffusion creep, respectively.

331

332 To calculate T_{flow} , we take our steady-state stresses (and corresponding pressures over the same
333 time intervals)—in addition to the parameters for dry dislocation creep, dry disGBS, and dry
334 diffusion creep of olivine, as summarized by Warren & Hansen (27)—and systematically vary T
335 to find the total strain rate, $\dot{\epsilon}$, that best matches our measured steady-state strain rates (Table S3).
336 For each steady-state point, we obtain three T_{flow} values using the stresses and pressures
337 calculated from the olivine (130), (131), and (112) diffraction peaks. Furthermore, for each
338 experiment we obtain steady-state measurements at up to three points: during initial deformation
339 within the quartz stability field, during deformation within the coesite stability field, and during
340 final deformation back in the quartz stability field. Thus, we derive up to nine T_{flow} values for
341 each experiment (see Table S3).

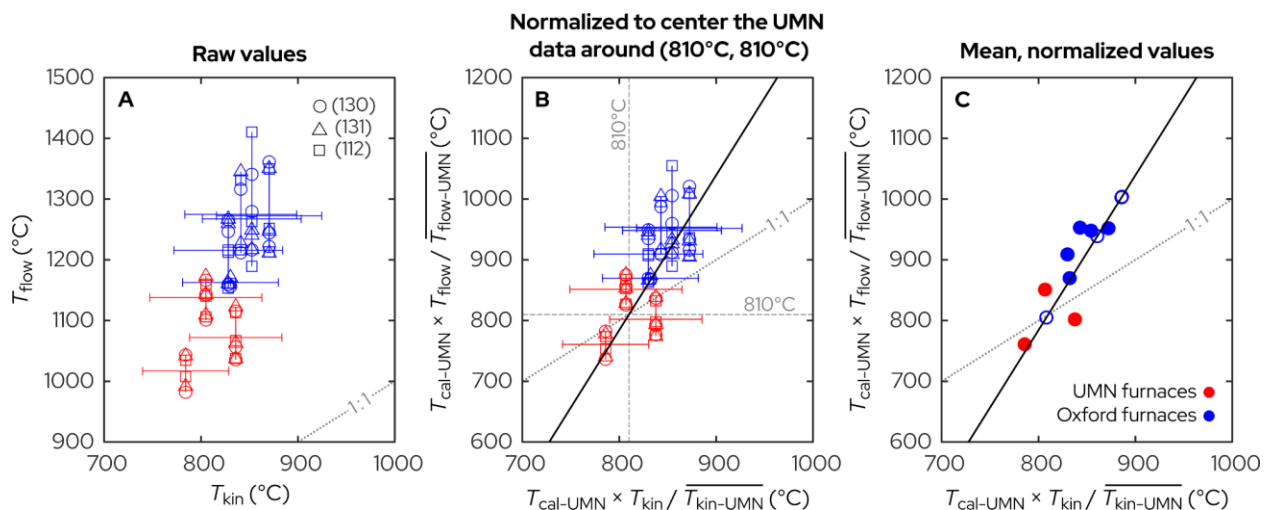
342

343 Because our XRD stress measurements are calculated using the elastic constants of olivine (and
344 their pressure and temperature derivatives), we must assume some initial value of temperature
345 for the XRD calculations. We therefore perform an iterative process in which an initial
346 temperature estimate (900°C) is used to calculate stress and pressure from the XRD data. These
347 stresses and pressures are used to derive an initial T_{flow} estimate for the Oxford-furnace
348 experiments (via Eqns. S5 and S6). The XRD data are then reprocessed using that initial T_{flow}
349 estimate—which also depends on T_{kin} as described below—to obtain refined stress, pressure, and
350 T_{flow} values. For San588, which we take as a representative experiment, we find that the T_{flow}
351 converges (within 5°C; *i.e.*, 0.5%) after only two iterations of this process. We therefore perform
352 only two iterations for every experiment containing an Oxford furnace. Furthermore, we
353

354 converge upon the same stresses (within 5 MPa; *i.e.*, 0.5%), pressures (within 0.15 GPa; *i.e.*,
 355 25%), and T_{flow} values (within 5°C; *i.e.*, 0.5%) even when varying the initial temperature
 356 estimate by $\pm 500^\circ\text{C}$.

357
 358 In Fig. S5, we compare our derived values of T_{kin} and T_{flow} . Reassuringly, we find a positive
 359 correlation between the two. Furthermore, we emphasize that these temperature estimates are
 360 entirely independent— T_{kin} is based on XRD peak intensity in the SiO_2 sample, whereas T_{flow} is
 361 derived from XRD peak position in the olivine sample. However, while the kinetics temperatures
 362 appear entirely reasonable—as stated above, the experiments with UMN furnaces yield T_{kin}
 363 values remarkably close to the temperature expected from our UMN furnace calibration ($T_{\text{cal-UMN}}$
 364 = 810°C)—our T_{flow} values seem unrealistically high. First, the experiments with UMN furnaces
 365 give T_{flow} values that are 190–560°C (20–65%) higher than the temperature expected from the
 366 UMN furnace calibration (red points in Fig. S5A). Second, some experiments with Oxford
 367 furnaces yield T_{flow} values that approach the melting point of our Ni strain markers (1450–
 368 1650°C over the range of pressures explored here). In other experiments using the same D-DIA
 369 apparatus, cell assembly, and materials (42, 43), we routinely imposed furnace power values of
 370 up to 280 W (*i.e.*, >30%, or nominally >300°C, greater than that applied here) without melting
 371 the Ni markers. At this time, we do not know the cause of the unrealistically high T_{flow} values.
 372 Although we have neglected the role of low-temperature plasticity in our T_{flow} calculations
 373 (Eqns. 5–6), the experiments that give the highest T_{flow} values exhibit very low differential
 374 stresses (<100 MPa), with minimal work hardening. Thus, the contribution of low-temperature
 375 plasticity in most experiments is likely negligible. Water is also an unlikely culprit. With wet
 376 olivine flow laws, we would have to invoke water concentrations far exceeding the water
 377 solubility of olivine to obtain T_{flow} values consistent with our T_{kin} values and calibrated
 378 temperatures. Finally, our differential stress—and, thus, T_{flow} —calculations are only minimally
 379 sensitive to temperature uncertainties. For example, varying the XRD data-processing
 380 temperature by $\pm 200^\circ\text{C}$ causes T_{flow} to vary by no more than $\pm 30^\circ\text{C}$ for San588.

381



382

383 **Fig. S5. Comparison of temperatures derived from the olivine flow law, T_{flow} , and**
384 **temperatures derived from the quartz→coesite transformation kinetics, T_{kin} .** (A) Raw
385 values. (B) Values normalized by the average T_{kin} and T_{flow} values of the UMN-furnace
386 experiments (red points), and then rescaled to center the UMN-furnace experiments around their
387 calibrated temperature, $T_{\text{cal-UMN}} = 810^{\circ}\text{C}$, derived from our UMN furnace calibration (Eqn. S2).
388 The black line shows a linear regression through the data (black line), which is forced to pass
389 through $T_{\text{cal-UMN}} = 810^{\circ}\text{C}$. (C) The mean normalized values for each experiment. Solid symbols
390 indicate experiments where both T_{kin} and T_{flow} are constrained. Hollow symbols indicate
391 experiments where either T_{kin} and T_{flow} could not be constrained—in these cases, we estimate the
392 missing temperature using the linear regression (solid black line) derived in (B).

393
394

395 To resolve the discrepancy between T_{kin} and T_{flow} , we normalize each T_{flow} value by the average
396 T_{flow} value of the UMN-furnace experiments ($\overline{T_{\text{flow-UMN}}} = 1083^{\circ}\text{C}$, 1085°C , and 1080°C , for
397 T_{flow} values obtained from stresses calculated for the (130), (131), and (112) olivine planes,
398 respectively), which were all performed at a furnace power of 209 W. For consistency, we also
399 normalize our T_{kin} values by the average T_{kin} value of the UMN-furnace experiments ($\overline{T_{\text{kin-UMN}}}$
400 $= 808^{\circ}\text{C}$). We then rescale the normalized values (*i.e.*, convert back to units of degrees Celsius)
401 by multiplying by the calibration temperature of the UMN-furnace experiments, $T_{\text{cal-UMN}} =$
402 810°C . The normalized, rescaled data are plotted in Fig. S5B. Note that the UMN-furnace
403 experiments are centered around 810°C (*i.e.*, $T_{\text{cal-UMN}}$).

404
405 To obtain a single temperature estimate for each experiment, we take a simple arithmetic average
406 of our mean normalized, rescaled T_{kin} and T_{flow} values (Fig. S5C). However, for some
407 experiments we were unable to determine either T_{kin} (San467, San552, San568) or T_{flow} (San506)
408 due to insufficient data. To aid in constraining the temperature of these experiments, we perform
409 a linear regression through the normalized, rescaled T_{kin} and T_{flow} values, forcing the regression
410 to pass through $T_{\text{cal-UMN}} = 810^{\circ}\text{C}$ (Fig. S5B). The missing temperature is then derived using this
411 relationship (see hollow points in Fig. S5C), which has a root-mean-square misfit of 58°C . We
412 therefore assume that our recalibrated temperatures are accurate to within $\pm 60^{\circ}\text{C}$.

413

414 Experiment Procedure

415 In each experiment, samples were pressurized to 1–2 GPa confining pressure with the differential
416 rams fully retracted (following the ~ 5 GPa cold press described above). Pressurization typically
417 introduced some differential stress (< 500 MPa), which we relaxed by annealing the samples for
418 10–30 minutes at 209 W (nominally 800 – 900°C). XRD patterns were monitored throughout the
419 anneal to verify 1) that the differential stresses became fully relaxed and 2) that the SiO_2 sample
420 remained within the quartz stability field. In non-hydrostatic experiments, the differential rams
421 were then advanced (at the syringe pump rates listed in Table S1) to begin deforming the quartz
422 and olivine samples via uniaxial shortening. Once the quartz and olivine samples were deforming

423 at a steady state (with the exception of San574, which even after 11% axial strain did not reach
424 state-state), the main ram was steadily advanced to begin increasing the confining pressure. In
425 most experiments, hydraulic load on the main ram was increased at a rate of 0.018–0.037 tons
426 per second, corresponding to a pressure ramp rate of 2–5 MPa/s (Table S1). However, one
427 experiment (San585) was pressurized at ~0.5 MPa/s.

428
429 Upon reaching the coesite stability field, we waited for the quartz→coesite transformation to
430 reach completion, and for the SiO₂ and olivine samples to reach steady-state, before reducing
431 pressure to return to the quartz stability field. Note that in both runs performed at our highest
432 deformation rate (0.01 mm/s differential ram syringe pump rate), we stopped the experiments in
433 the coesite stability field to avoid the D-DIA anvils coming into contact due to the large
434 shortening strains reached. In all other experiments, we again waited for the coesite→quartz
435 transformation to reach completion, and for the SiO₂ and olivine samples to reach steady-state,
436 before stopping the experiment. Each experiment was stopped by cutting power to the graphite
437 furnace and stopping the differential rams in quick succession. The load on the main ram was
438 then removed to depressurize the assembly, keeping the differential rams in their advanced
439 position to maintain a small positive deviatoric stress on the sample, and thereby minimize
440 decompression cracking.

441 **Supplementary Text**

442

443 Viscosity calculation

444

445 Viscosity, η (Fig. 2) is calculated as:

446

447
$$\eta = \sigma / \dot{\epsilon}$$
 Eqn. S7

448

449 where σ is differential stress and $\dot{\epsilon}$ is the true (logarithmic) axial strain rate (hereafter referred to
450 simply as “strain rate”). At each time interval, we obtain three values of viscosity: one for each
451 of the F_{090} diffraction peaks, (130), (131), and (112). Strain rate is calculated as the first
452 derivative of true (logarithmic) axial strain with respect to time. However, due to experimental
453 uncertainties on strain, the raw strain-rate measurements are relatively noisy. Therefore, we first
454 smoothed the strain data using a Gaussian-weighted moving average filter. The smoothing
455 window for each experiment varied between 2 and 30 measurements, depending on the length of
456 the experiment and strain rates involved (*i.e.*, larger smoothing windows for long, slow
457 experiments).

458

459 Weakening factor (F_W), and rate factor (F_R) calculation

460

461 To examine the rate dependence of weakening, we calculate two scaling factors: the weakening
462 factor, F_W , and the rate factor, F_R . The weakening factor is defined as the amplitude of the
463 viscosity drop observed during the quartz→coesite transformation (Fig. 2) or, more explicitly:

464

465
$$F_W = \eta_{\text{expected}} / \eta_{\text{measured}}$$
 Eqn. S8

466

467 where η_{expected} is the steady-state viscosity expected for a 50-50 vol.% mixture of quartz and
468 coesite, calculated as the geometric mean of the quartz and coesite viscosities (measured in the
469 steady-state portions of each experiment), while η_{measured} is the viscosity measured mid-way
470 through the quartz→coesite transformation. To avoid propagating artifacts introduced by our
471 strain-rate smoothing procedure, we calculate these viscosities using strain rates derived via
472 linear regression through the raw axial strain data. Differential stress is then extracted over the
473 same time interval and used to calculate viscosity (Eqn. S7). For each experiment, we obtain
474 three values of F_W representing the viscosity drop associated with each of the (130), (131), and
475 (112) diffraction peaks in olivine.

476

477 The rate factor, F_R , on the other hand, represents the ratio of the transformation rate, $\dot{\epsilon}_{\text{transform}}$,
478 and deformation rate, $\dot{\epsilon}_{\text{deform}}$:

479

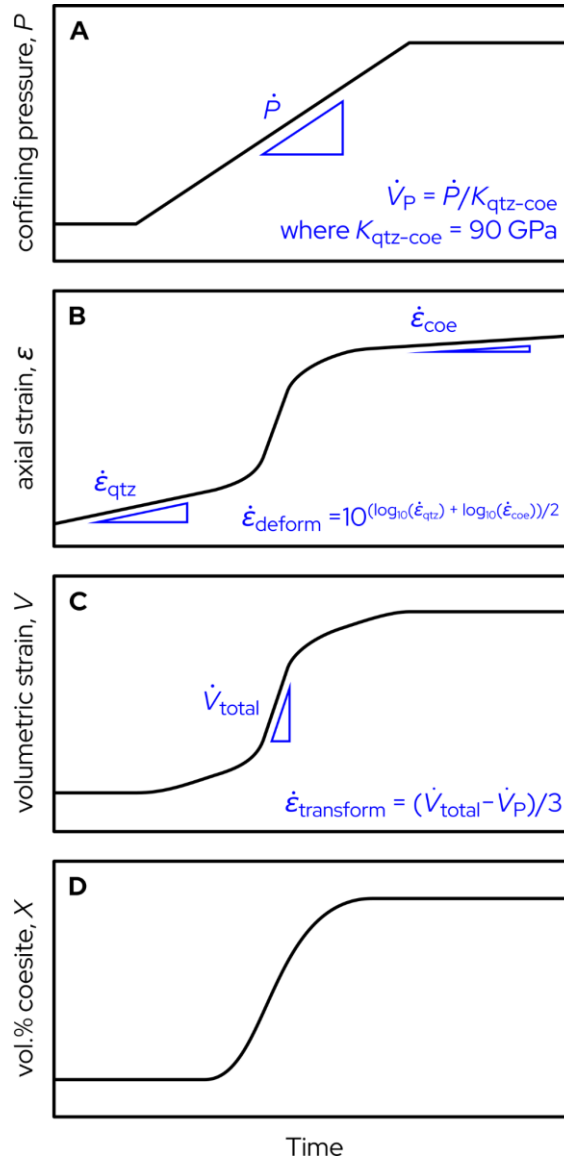
480
$$F_R = \dot{\epsilon}_{\text{transform}} / \dot{\epsilon}_{\text{deform}}$$
 Eqn. S9

481 where $\dot{\epsilon}_{\text{transform}}$ is taken as the component of the transient volumetric strain rate resolved along
 482 the vertical (shortening) direction. More plainly, $\dot{\epsilon}_{\text{transform}}$ is defined as one third of the
 483 volumetric strain rate during the transformation (assuming for simplicity that the quartz→coesite
 484 volume change is isotropic). Note, however, that we must first account for the change in volume
 485 caused by the change in pressure during the transformation—to achieve this, we divide the
 486 pressure ramp rate (in GPa/s) by an assumed average bulk modulus for quartz and coesite of 90
 487 GPa (neglecting elastic softening effects due to the phase transformation for simplicity). We then
 488 subtract the resulting volumetric strain rate from the measured (total) volumetric strain rate. The
 489 derivation of $\dot{\epsilon}_{\text{transform}}$ is schematically illustrated in Fig. S6.

491
 492 Meanwhile, the deformation rate, $\dot{\epsilon}_{\text{deform}}$, is taken as the geometric mean steady-state strain rate
 493 of quartz and coesite; that is, the background strain rate (Fig. S6). Errors on F_R are estimated as
 494

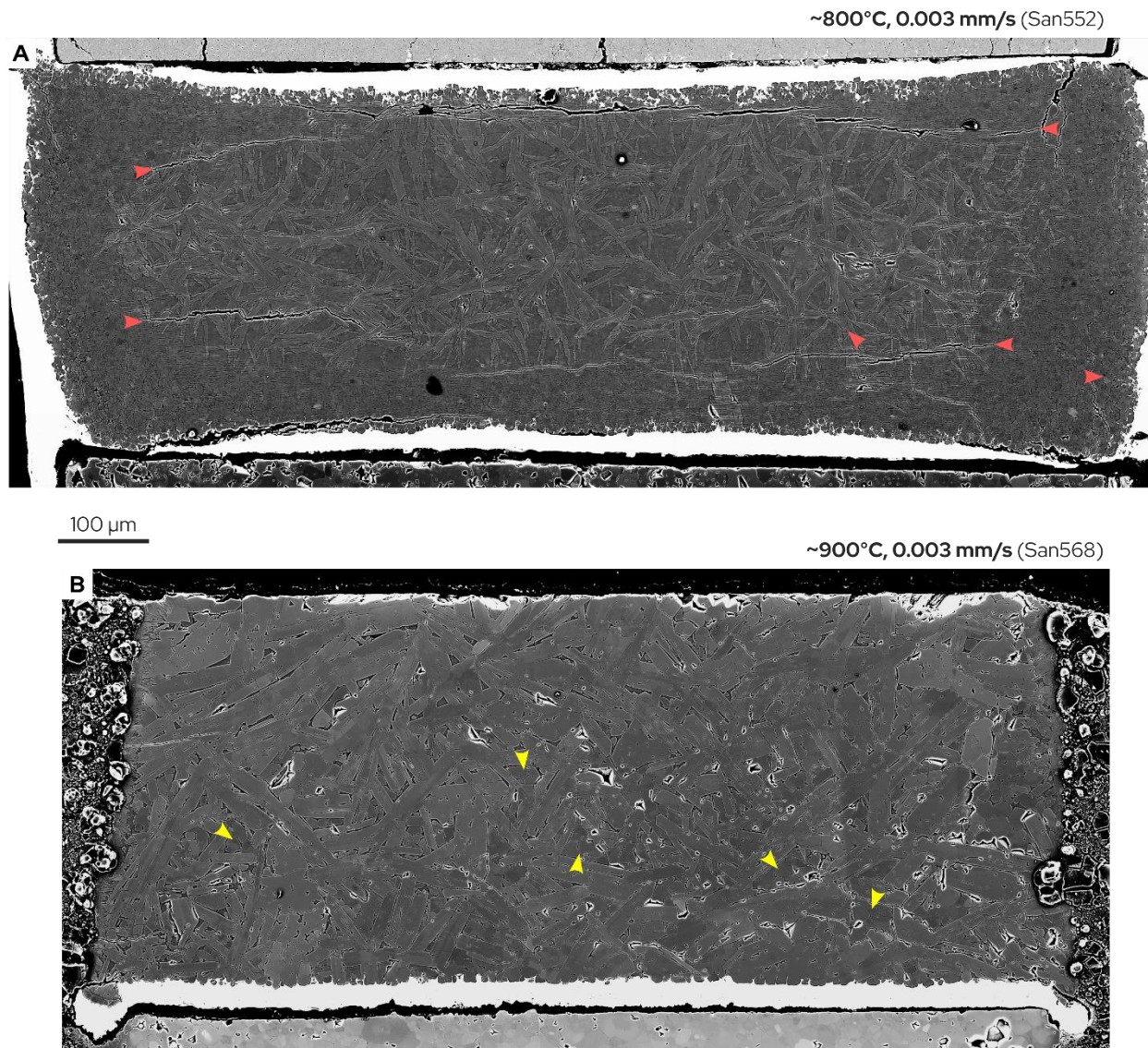
$$\Delta F_R = \sqrt{\Delta \dot{\epsilon}_{\text{transform}}^2 + \Delta \dot{\epsilon}_{\text{deform}}^2} \quad \text{Eqn. S10}$$

496
 497 where Δ denotes error. The transformation rate error, $\Delta \dot{\epsilon}_{\text{transform}}$, is calculated by conservatively
 498 assuming that we can resolve a volumetric strain no smaller than 5×10^{-4} over a typical imaging
 499 period of 1 radiograph per 20 seconds (as a reminder, the volumetric strain resolution is 10^{-4})—
 500 this yields a volumetric strain rate resolution $\Delta \dot{\epsilon}_{\text{transform}}$ of 2.5×10^{-4} . Similarly, we
 501 conservatively estimate that we can resolve an axial strain of no less than 5×10^{-5} over a period
 502 of 20 seconds (the axial strain resolution is actually 10^{-5}), providing an axial strain rate
 503 resolution, $\Delta \dot{\epsilon}_{\text{deform}}$ of 2.5×10^{-5} . These values are both larger than the observed noise floor of
 504 our strain-rate measurements, verifying that they are indeed conservative estimates of the strain
 505 rate uncertainty. Eqn. S10 further ensures an upper estimate on ΔF_R since it assumes constructive
 506 superposition of $\Delta \dot{\epsilon}_{\text{transform}}$ and $\Delta \dot{\epsilon}_{\text{deform}}$. In reality, these errors are likely negligible for all
 507 experiments presented here.



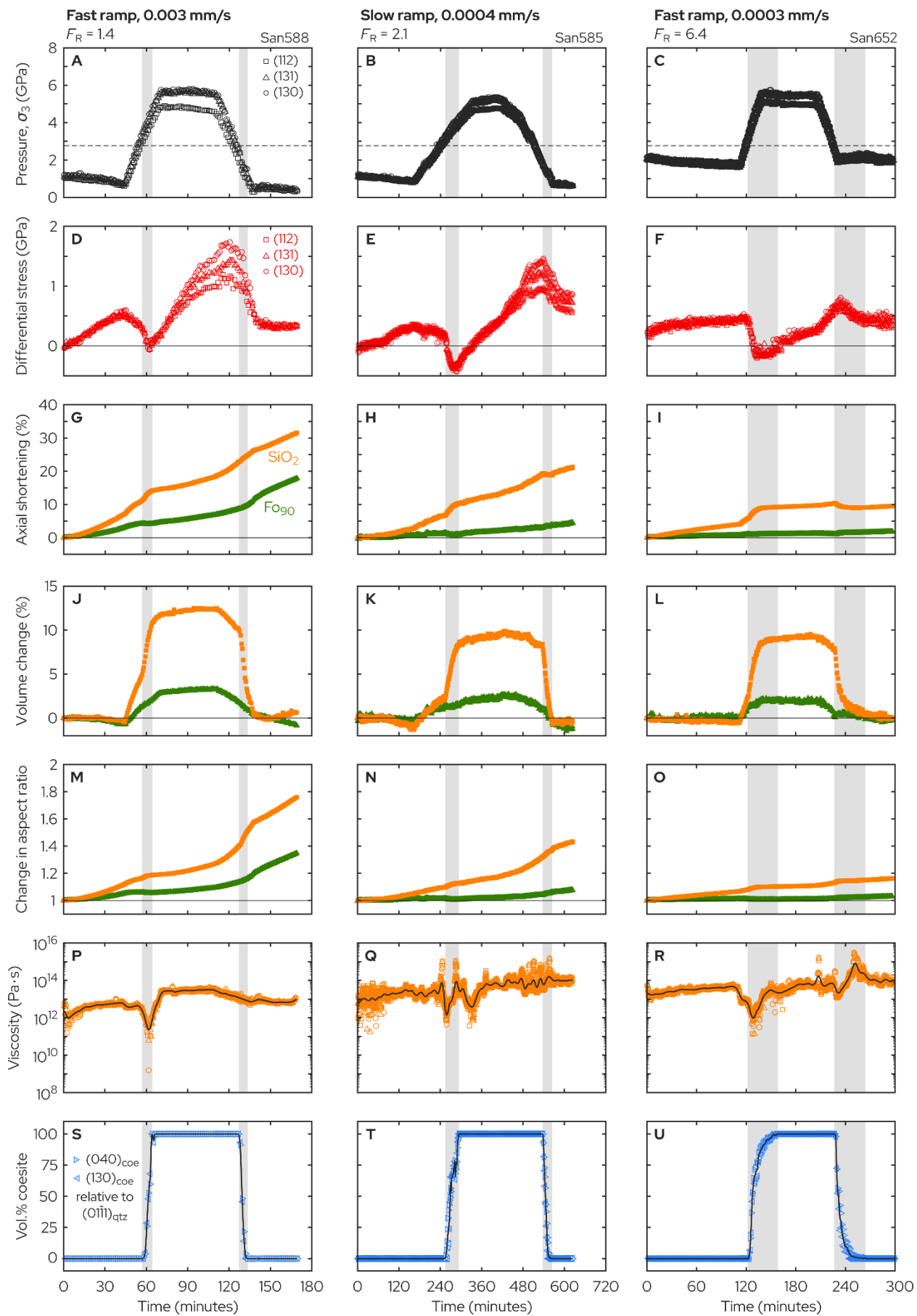
508
509

510 **Fig. S6. Derivation of the transformation rate factor, F_R .** Schematic plots of (A) confining
511 pressure, P , (B) axial strain, ϵ , (C) volumetric strain, V , and (D) coesite volume fraction, X , as a
512 function of time. F_R represents the ratio between the transformation rate, $\dot{\epsilon}_{\text{transform}}$, and the
513 deformation rate, $\dot{\epsilon}_{\text{deform}}$ (Eqn. S9). $\dot{\epsilon}_{\text{deform}}$ is given as the geometric mean of the steady-state
514 strain rates of quartz and coesite (B). Meanwhile, $\dot{\epsilon}_{\text{transform}}$ is given as one third of the
515 volumetric strain rate during the transformation, \dot{V}_{total} (C), minus the volumetric strain rate due
516 to the imposed change in pressure, \dot{V}_P (A). In principle, $\dot{\epsilon}_{\text{transform}}$ represents an effective axial
517 strain rate due to the quartz \rightarrow coesite volume change.



518
519

520 **Fig. S7. Microstructure of samples quenched mid-way through the quartz→coesite phase**
 521 **transformation under non-hydrostatic conditions.** Backscatter electron (BSE) images
 522 collected using a Zeiss Supra 40VP FEG-SEM at the Marine Biological Laboratory, Woods
 523 Hole, MA. (A) Sample San552, conducted at ~800°C and 0.003 mm/s differential ram syringe
 524 pump rate (~50% coesite), and (B) sample San568, conducted at ~900°C and also 0.003 mm/s
 525 differential ram syringe pump rate (~90% coesite). The shortening direction is vertical for both
 526 samples. The lighter phase is coesite; the darker phase is quartz. Red arrows indicate
 527 decompression cracks, while yellow arrows indicate remnant quartz grains in San568.



529 **Fig. S8. Effect of pressure ramp rate on transformational weakening.** (A–C) Confining
530 pressure, σ_3 , (D–F) differential stress, $\sigma_1 - \sigma_3$, (G–I) axial strain, (J–L) volumetric strain, (M–O)
531 sample aspect ratio (diameter divided by width) relative to the initial sample shape, (P–R)
532 viscosity, and (S–U) coesite volume proportion as a function of time. Vertical gray bars represent
533 the time intervals over which both quartz and coesite peaks are present in the XRD spectra.
534 Orange squares and green triangles represent the SiO₂ sample and Fo₉₀ reference standard,
535 respectively, in (G–O). As a visual aid, a spline has been fit through the average of the viscosity
536 and volume proportion data in (P–U; black curves) All experiments were performed at graphite
537 furnace powers corresponding to a nominal temperature of 810°C. Pressure was ramped at a rate
538 of 2.2–3.2 MPa/s in San588 (left column) and San652 (right column), and 0.4–0.6 MPa/s in
539 San585 (middle column). The differential ram syringe pump rate (*i.e.*, deformation rate) is
540 indicated in units of mm/s above each column. The rate ratio, F_R (transformation rate divided by
541 deformation rate) increases from left to right.

542
543 Slab model

544
545 To explore the likelihood of transformational weakening on geological timescales, we calculate
546 the transformation and deformation rates of a downgoing slab passing through the mantle
547 transition zone (Fig. S9). Following Hosoya *et al.* (23), we calculate the progression of the
548 olivine-wadsleyite phase transformation for a slab descending at a rate of 12 cm/yr, with a
549 thermal gradient of 0.6 K/km. The volume fraction of transformed material, X , is calculated as

$$X = 1 - \exp \left[2S \int \dot{x}(z) dz \right]$$

552 **Eqn. S11**

553
554 where S is the grain boundary area of the parent phase, olivine (taken as $3.35/d$, where d is the
555 grain size of olivine), and $\dot{x}(z)$ is the growth rate at each increment of depth, z , given by

$$\dot{x} = BT C_{OH}^p \exp \left(-\frac{E_g + PV_g}{RT} \right) \left[1 - \exp \left(-\frac{\Delta E_r}{RT} \right) \right]$$

558 **Eqn. S12**

559
560 where B is a pre-exponential rate factor, T is absolute temperature, C_{OH} is water content in wt.
561 ppm H₂O, p is the water exponent of the phase transformation, E_g is the activation energy for
562 growth of the product phase (wadsleyite), P is pressure, V_g is the activation volume for growth, R
563 is the gas constant, and ΔE_r is the free energy change of the transformation (taken as $\Delta P \Delta V$,
564 where ΔP is the overpressure relative to the phase boundary, and ΔV is the difference in specific
565 volume between the parent and product phase). Overpressure is calculated as the difference
566 between the pressure at any given depth and the pressure expected for the olivine-wadsleyite

567 phase boundary at corresponding pressure-temperature conditions. Pressure is calculated using
 568 the relation

569 $P = \rho g z$ (where ρ is density and g is gravitational acceleration), while the phase boundary is
 570 defined as $P = 9.3 + 0.0036T$, with temperature, T , in units of degrees Celsius (54). The kinetic
 571 parameter values, boundary conditions, and model constants are provided in Table S4.

572

573 Meanwhile, we calculate deformation rates in the downgoing slab using rheological flow laws
 574 for olivine. Given the relatively low temperatures, high stresses, and coarse olivine grain size, it
 575 is assumed that deformation proceeds via low-temperature plasticity and dislocation creep:

576

$$\dot{\epsilon}_{\text{deform}} = \dot{\epsilon}_{\text{LTP}} + \dot{\epsilon}_{\text{dis}} \quad \text{Eqn. S13}$$

577

$$\dot{\epsilon}_{\text{LTP}} = A_{\text{LTP}} \rho_d \exp\left(-\frac{E_{\text{LTP}}}{RT}\right) \sinh\left(\frac{E_{\text{LTP}}}{RT} \frac{\sigma - \sigma_p}{\Sigma}\right) \quad \text{Eqn. S14}$$

581

582

$$\dot{\epsilon}_{\text{dis}} = A_{\text{dis}} \sigma^n C_{\text{OH}}^r \exp\left(-\frac{E_{\text{dis}} + PV_{\text{dis}}}{RT}\right) \quad \text{Eqn. S15}$$

583

584

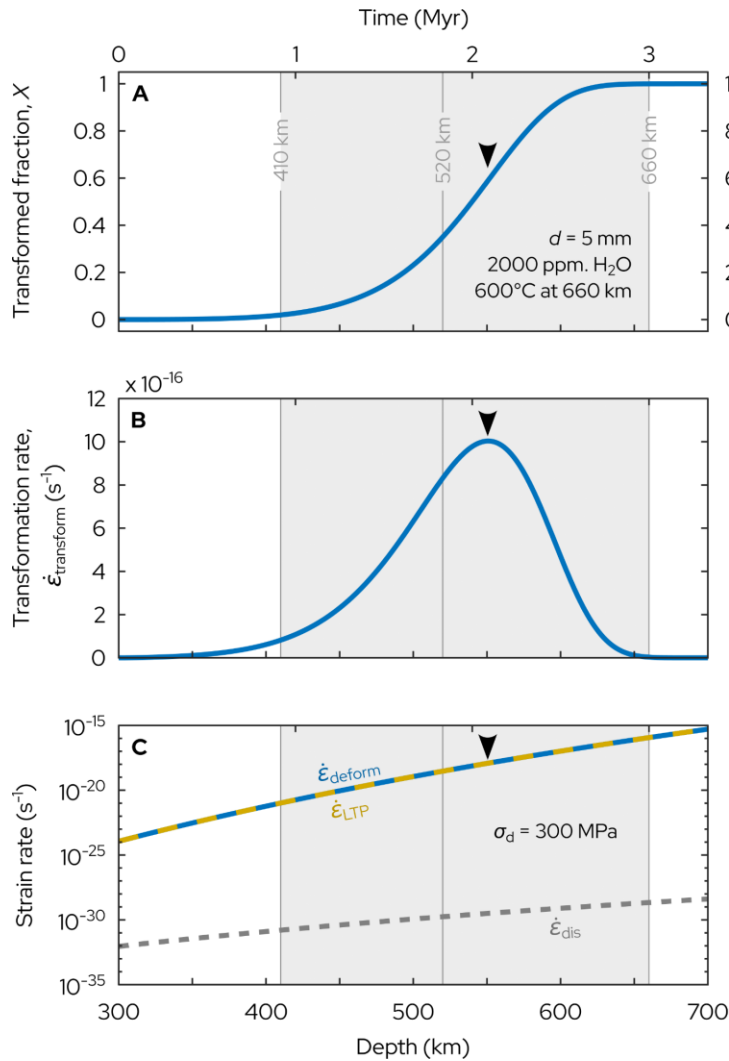
585 where the subscripts “LTP” and “dis” denote low-temperature plasticity and dislocation creep,
 586 respectively, $\dot{\epsilon}$ is strain rate, A is a pre-exponential rate constant, ρ_d is dislocation density, E
 587 is activation energy, σ is differential stress, σ_p is the backstress due to long-range dislocation
 588 interactions, Σ is the Peierls stress, n is the stress exponent, and r is the water exponent. For low-
 589 temperature plasticity, we use a flow law of the form proposed by Hansen *et al.* (42), with
 590 parameters applicable to the onset of plastic deformation—that is, at the yield point, prior to
 591 work hardening and the development of a backstress. Note that we use these parameters because
 592 steady-state low-temperature plasticity is expected only for applied stresses exceeding 1.8 GPa,
 593 whereas slab stress estimates are on the order of a few hundred MPa at most (28–30). For
 594 dislocation creep, we use the wet flow law parameters from Hirth & Kohlstedt (26) with the
 595 revised A value from Warren & Hansen (27). The flow law parameters are provided in Table S4.

596

597 At each given depth, X is calculated and converted to a volumetric strain (Fig. S9A) assuming
 598 that there is a 10% density increase (*i.e.*, 10% volume contraction) associated with the olivine-
 599 wadsleyite phase transition. By taking the first time derivative of the true (logarithmic)
 600 volumetric strain, we obtain the volumetric strain rate as a function of depth. As above, the
 601 transformation rate, $\dot{\epsilon}_{\text{transform}}$ (Fig. S9B) is taken as one third of the volumetric strain rate (to
 602 obtain the effective strain rate produced by the transformation along the direction of maximum
 603 principal stress), assuming for simplicity that the volume change is isotropic. Meanwhile, we
 604 calculate the deformation rate, $\dot{\epsilon}_{\text{deform}}$, as a function of depth using Eqns. S13–S15 (Fig. S9C).

605

606 For each combination of temperature, water content, and stress boundary conditions, we obtain a
 607 single value of the rate factor, F_R —that is, the ratio of the transformation and deformation
 608 rates—by finding the peak transformation rate (Fig. S9B, black arrow) and then taking the
 609 deformation rate at the same depth (Fig. S9C, black arrow). In the example provided in Fig. S9,
 610 we obtain a maximum value for $\dot{\epsilon}_{\text{transform}}$ of $1.0 \times 10^{-15} \text{ s}^{-1}$, and $\dot{\epsilon}_{\text{deform}} = 1.2 \times 10^{-18} \text{ s}^{-1}$ at the
 611 same depth (550 km), giving a rate factor value of $F_R = 830$ for this set of conditions (600°C slab
 612 temperature at the 660 km discontinuity, 2000 wt. ppm H_2O , 300 MPa differential stress).



613

614 **Fig. S9. Model of transformation and deformation rates in a downgoing slab.** (A) Volume
 615 fraction of material transformed from olivine to wadsleyite, X , and the associated volumetric
 616 strain, as a function of depth. (B) First derivative of the volumetric strain from (A), divided by
 617 three to obtain the effective strain rate produced by the transformation along the direction of
 618 maximum principal stress (assuming that the volume change is isotropic). (C) Olivine strain rate,
 619 $\dot{\epsilon}_{\text{deform}}$, given as the sum of the strain rates due to low-temperature plasticity (subscript “LTP”)
 620 and dislocation creep (subscript “dis”) as a function of depth, for a differential stress of 300 MPa.

621 **Table S1.** Experiment run conditions

Experiment #	Top sample	Bottom sample	Graphite furnace origin	Furnace power (W)	Temperature (°C)	Differential ram syringe pump rate (mm/s)	Pressure ramp rate, up / down (MPa/s)	Rate factor, F_R	Weakening factor, F_W		
									(112)	(131)	(130)
<i>Hydrostatic ($\sigma_1 \approx \sigma_2 \approx \sigma_3$)</i>											
San506	PI-2056	LT-QHP	Oxford	188	945 [†]	0	2.6 / 2.7	N/A	N/A	N/A	N/A
<i>Non-hydrostatic ($\sigma_1 > \sigma_2 \approx \sigma_3$)</i>											
San467*	PI-2056	LT-QHP	Oxford	209	944 [†]	0.003	4.6 / 3.6	4.4 ± 0.12	99	97	25
San537	LT-QHP	PI-2056	Oxford	167	892 [†]	0.003	2.6 / 2.9	2.3 ± 0.18	16	14	26
San538	LT-QHP	PI-2056	Oxford	167	903 [†]	0.01	3.1 / N/A	0.48 ± 0.19	0.72	0.67	0.64
San558	PI-2094	LT-QHP	Oxford	167	869 [†]	0.0003	2.8 / 3.3	15 ± 0.96	39	28	26
San572	PI-2094	LT-QHP	Oxford	198	851 [†]	0.01	2.5 / N/A	0.49 ± 0.25	0.48	0.47	0.48
San574	PI-2094	LT-QHP	Oxford	209	901 [†]	0.0003	2.6 / 2.4	99 ± 4.4	49	47	46
San585	LT-QHP	PT-1616	UMN	209	810 [‡]	0.0004	0.41 / 0.60	2.1 ± 1.2	11	7.9	7.6
San588	PT-1616	LT-QHP	UMN	209	810 [‡]	0.0003	3.1 / 3.2	1.4 ± 0.25	13	11	14
San652	PT-1616	LT-QHP	UMN	209	810 [‡]	0.003	2.4 / 2.2	6.4 ± 1.0	105	23	28
<i>Mid-transformation quench (non-hydrostatic)</i>											
San552	PI-2094	LT-QHP	Oxford	209	807 [†]	0.003	1.3 / N/A	N/A	N/A	N/A	N/A
San568	LT-QHP	PI-2094	Oxford	209	900 [†]	0.003	2.9 / N/A	N/A	N/A	N/A	N/A

* Experiment performed without initial room-temperature pressure cycle (see Materials and Methods for details)

† Temperature inferred from the quartz→coesite transformation kinetics and/or olivine flow strength (see Materials and Methods for details). ± 60°C uncertainty.

‡ Temperature calculated using power-temperature calibration (Fig. S3; Eqn. S2). ± 20°C uncertainty.

623 **Table S2.** Temperature calibration data—quartz→coesite transformation kinetics

Experiment #	Olivine sample	Graphite furnace origin	Furnace power (W)	Avrami rate parameter, k (s^{-1})	Temperature estimate, T_{kin} ($^{\circ}C$)
<i>Hydrostatic ($\sigma_1 \approx \sigma_2 \approx \sigma_3$)</i>					
San506	PI-2056	Oxford	188	4.89×10^{-3}	884 ± 52
<i>Non-hydrostatic ($\sigma_1 > \sigma_2 \approx \sigma_3$)</i>					
San467*	PI-2056	Oxford	209	-	-
San537	PI-2056	Oxford	167	3.76×10^{-3}	870 ± 54
San538	PI-2056	Oxford	167	2.11×10^{-3}	841 ± 58
San558	PI-2094	Oxford	167	1.62×10^{-3}	828 ± 56
San572	PI-2094	Oxford	198	1.70×10^{-3}	830 ± 49
San574	PI-2094	Oxford	209	2.65×10^{-3}	852 ± 51
San585	PT-1616	UMN	209	6.27×10^{-4}	784 ± 44
San588	PT-1616	UMN	209	9.95×10^{-4}	805 ± 58
San652	PT-1616	UMN	209	1.90×10^{-3}	836 ± 48
<i>Mid-transformation quench (non-hydrostatic)</i>					
San552*	PI-2094	Oxford	209	-	-
San568*	PI-2094	Oxford	209	-	-

* Not enough data points for Avrami regression

625 **Table S3.** Temperature calibration data—olivine flow law

Experiment #	Graphite furnace origin	Olivine sample	Furnace power (W)	Phase*	Steady-state strain rate, olivine (s ⁻¹)	Steady-state differential stress (MPa)			Confining pressure (GPa)			Temperature estimate, T_{flow} (°C)		
						(112)	(131)	(130)	(112)	(131)	(130)	(112)	(131)	(130)
<i>Non-hydrostatic ($\sigma_1 > \sigma_2 \approx \sigma_3$)</i>														
San467	Oxford	PI-2056	209	quartz-1	7.94×10^{-6}	50	89	-41	1.68	1.71	2.00	1388	1333	-
				coesite [†]	6.97×10^{-6}	-	-	-	-	-	-	-	-	-
				quartz-2	2.46×10^{-5}	119	152	183	1.56	1.75	1.84	1350	1329	1311
San537	Oxford	PI-2056	167	quartz-1	1.70×10^{-5}	322	365	378	2.30	2.51	2.54	1252	1247	1244
				coesite	1.57×10^{-5}	415	524	489	5.39	6.04	6.13	1350	1350	1361
				quartz-2	1.29×10^{-5}	295	310	291	1.45	1.53	1.61	1213	1211	1222
San538	Oxford	PI-2056	167	quartz-1	1.29×10^{-5}	449	455	534	2.57	2.85	2.88	1217	1227	1212
				coesite	3.15×10^{-5}	681	819	1065	5.57	6.42	6.42	1332	1345	1316
San558	Oxford	PI-2094	167	quartz-1	3.69×10^{-6}	115	64	51	2.00	2.84	2.34	1213	1267	1266
				coesite	1.10×10^{-8}	10	19	15	5.72	7.38	6.88	1154	1161	1160
				quartz-2	3.83×10^{-6}	67	45	45	0.89	1.71	1.21	1216	1260	1247
San572	Oxford	PI-2094	198	quartz-1 [†]	8.91×10^{-5}	-	-	-	-	-	-	-	-	-
				coesite	2.24×10^{-5}	1106	1353	1611	3.47	4.20	4.22	1161	1171	1156
San574	Oxford	PI-2094	209	quartz-1	2.00×10^{-6}	18	25	15	1.18	1.35	1.45	1263	1249	1280
				coesite	-1.19×10^{-6}	-324	-261	-285	5.25	5.99	6.14	1189	1217	1216
				quartz-2	1.88×10^{-6}	1	23	4	0.81	0.92	1.03	1411	1241	1341

626

Experiment #	Graphite furnace origin	Olivine sample	Furnace power (W)	Phase*	Steady-state strain rate, olivine (s ⁻¹)	Steady-state differential stress (MPa)			Confining pressure (GPa)			Temperature estimate, T_{flow} (°C)		
						(112)	(131)	(130)	(112)	(131)	(130)	(112)	(131)	(130)
San585	UMN	PT-1616	209	quartz-1	1.31×10^{-6}	344	305	306	0.83	0.84	0.9	1035	1042	1043
				coesite [†]	1.07×10^{-6}	-	-	-	-	-	-	-	-	-
				quartz-2	1.97×10^{-6}	585	737	858	0.62	0.63	0.66	1008	992	982
San588	UMN	PT-1616	209	quartz-1	2.19×10^{-5}	482	490	545	0.66	0.78	0.79	1106	1109	1101
				coesite	1.12×10^{-5}	980	1198	1401	4.62	5.52	5.63	1160	1173	1166
				quartz-2	2.98×10^{-5}	324	326	334	0.39	0.47	0.52	1140	1143	1143
San652	UMN	PT-1616	209	quartz-1	9.21×10^{-7}	397	424	453	1.66	1.76	1.84	1038	1037	1036
				coesite	4.70×10^{-7}	222	220	271	4.95	5.41	5.47	1113	1123	1116
				quartz-2	1.49×10^{-7}	359	427	485	1.92	2.1	2.12	1067	1063	1056
<i>Mid-transformation quench (non-hydrostatic)</i>														
San552	Oxford	PI-2094	209	quartz-1	1.34×10^{-5}	977	1185	1367	1.63	1.99	2.00	1083	1080	1068
San568	Oxford	PI-2094	209	quartz-1	1.49×10^{-5}	168	69	111	1.07	1.07	1.27	1221	1286	1259

* “quartz-1” indicates deformation during the initial stage in the quartz stability field; “coesite” indicates deformation in the coesite stability field; “quartz-2” indicates deformation during the final stage in the quartz stability field

† Steady-state not reached

629 **Table S4.** Slab model parameters

Parameter	Description	Value	Units
<i>Boundary conditions and constants</i>			
Z	depth	variable	m
dT/dz	thermal gradient	0.6×10^{-3}	K/m
dz/dt	subduction rate	0.12	m/yr
T_{660}	absolute temperature at 660 km discontinuity	873–1473	K
C_{OH}	water content	1–10000	wt. ppm H ₂ O
σ	differential stress	1–300	$\times 10^6$ Pa
ρ	density	3600*	kg/m ³
g	gravitational acceleration	9.81	m/s ²
P	pressure	$\rho g z$	Pa
R	gas constant	8.314	J mol ⁻¹ K ⁻¹
<i>Olivine-wadsleyite phase transformation (intercrystalline nucleation and growth)[†]</i>			
d	grain size of parent phase	0.005	m
S	grain boundary area of parent phase	$3.35/d$	m ² /m ³
B	pre-exponential rate constant	$\exp(-18)$	m s ⁻¹ K ⁻¹ wt. ppm H ₂ O ^{-p}
p	water exponent	3.2	-
E_g	activation energy	274	$\times 10^3$ J/mol
V_g	activation volume	3.3	$\times 10^{-6}$ m ³ /mol
ΔV	change in specific volume	3.0^{\ddagger}	$\times 10^{-6}$ m ³ /mol
ΔE_r	free energy change	$\Delta P/\Delta V$	J/mol
<i>Olivine deformation, low temperature plasticity[§]</i>			
A_{LTP}	pre-exponential rate constant	$10^{-1.32}$	m ² /s
ρ_d	dislocation density	10^{10}	m/m ³
E_{LTP}	activation enthalpy	450	$\times 10^3$ J/mol
σ_p	backstress	0	$\times 10^6$ Pa
Σ	Peierls stress	3100	$\times 10^6$ Pa

630

631 **Table S4 cont.**

Parameter	Description	Value	Units
<i>Olivine deformation, wet dislocation creep</i> [¶]			
A_{dis}	pre-exponential rate constant	570 [#]	$\text{s}^{-1} \text{Pa}^{-n} \text{wt. ppm H}_2\text{O}^{-p}$
n	stress exponent	3.5	-
r	water exponent	1.2	-
E_{dis}	activation energy	480	$\times 10^3 \text{ J/mol}$
V_{dis}	activation volume	11	$\times 10^{-6} \text{ m}^3/\text{mol}$

* Density of San Carlos olivine at ~12 GPa (45)

† Values from Hosoya *et al.* (23) unless stated otherwise

‡ Values from Mohiuddin & Karato (30)

§ Values from Warren & Hansen (27)

¶ Values from Hirth & Kohlstedt (26) unless stated otherwise

As revised by Warren & Hansen (27)

632

633

634 **Data S1–S12.** Mechanical data (separate files). Comma-separated value (CSV) files with the
635 time (column A), confining pressure (B–C), differential stress (E–G), SiO₂ sample shape (H–J),
636 SiO₂ axial strain (K), SiO₂ volumetric strain (L), Fo₉₀ stress sensor shape (M–O), Fo₉₀ axial
637 strain (P), Fo₉₀ volumetric strain (Q), and coesite volume percentages (R–S) for each experiment
638 listed in Table 1. Pressures, stresses, and phase proportions were obtained from X-ray
639 diffraction, while sample strains were obtained via X-ray radiography. Diffraction spectra and
640 radiographs were collected alternately.

641

642 **Data S13.** Slab model (separate file). MATLAB[®] model used to investigate the transformation
643 kinetics and strain rates of olivine during descent in a downgoing slab (Figs. 4 and S9). Written
644 and tested using MATLAB[®] version R2022b. See *Supplementary Text* for full description.